ANNUAL REVIEWS

Annual Review of Condensed Matter Physics

Bubbly and Buoyant Particle–Laden Turbulent Flows

Varghese Mathai,[1] Detlef Lohse,[2,3] and Chao Sun[4]

[1]School of Engineering, Brown University, Providence, Rhode Island 02912, USA

[2]Physics of Fluids Group, Max Planck–University of Twente Centre for Complex Fluid Dynamics; MESA+ Institute; and Department of Science and Technology, University of Twente, 7500 AE Enschede, The Netherlands

[3]Max Planck Institute for Dynamics and Self-Organization, 37077 Göttingen, Germany

[4]Center for Combustion Energy, Key Laboratory for Thermal Science and Power Engineering of Ministry of Education, and Department of Energy and Power Engineering, Tsinghua University, Beijing 100084, China; email: chaosun@tsinghua.edu.cn

ANNUAL REVIEWS CONNECT

www.annualreviews.org

- Download figures
- Navigate cited references
- Keyword search
- Explore related articles
- Share via email or social media

Keywords

bubbles, buoyant particles, Lagrangian dynamics, wake–turbulence interaction, bubble-induced turbulence, two-way coupling

Abstract

Fluid turbulence is commonly associated with stronger drag, greater heat transfer, and more efficient mixing than in laminar flows. In many natural and industrial settings, turbulent liquid flows contain suspensions of dispersed bubbles and light particles. Recently, much attention has been devoted to understanding the behavior and underlying physics of such flows by use of both experiments and high-resolution direct numerical simulations. This review summarizes our present understanding of various phenomenological aspects of bubbly and buoyant particle–laden turbulent flows. We begin by discussing different dynamical regimes, including those of crossing trajectories and wake-induced oscillations of rising particles, and regimes in which bubbles and particles preferentially accumulate near walls or within vortical structures. We then address how certain paradigmatic turbulent flows, such as homogeneous isotropic turbulence, channel flow, Taylor–Couette turbulence, and thermally driven turbulence, are modified by the presence of these dispersed bubbles and buoyant particles. We end with a list of summary points and future research questions.

1. INTRODUCTION AND OBJECTIVES OF REVIEW

Turbulent multiphase flows are common in nature and industry. Typical examples are pollutants dispersed in the atmosphere, air bubbles and plankton in the oceans, sediment-laden river flows, and catalytic particles and bubble columns in process technology. In all of these examples, the particles of the dispersed phase have a different mass density from that of the carrier phase. When the dispersed particle is lighter than the carrier fluid element, there may be major consequences for the kinematics and dynamics of both phases, often triggering a multitude of flow modifications. Many of these flow modifications can be viewed as originating from the inherent buoyancy of the bubbles and light particles, which renders them capable of adding energy over a range of scales while ascending through the turbulent flow. These flow modifications have decisive roles in many natural phenomena, for example, in the collective dynamics of buoyant zooplankton undergoing diel vertical migration (e.g., 1, 2); in bubble-induced mixing in the upper oceans (e.g., 3); and in engineering applications of drag reduction, heat transfer, and mixing (e.g., 4–6).

The subject of dispersed particles in turbulent flows has been studied extensively from the perspective of small (inertial) particles. For reviews of experimental and numerical techniques for particle-laden flows, see References 7–13. Over the past couple of decades, researchers have gained much insight into particle dynamics and flow modulations at various scales of turbulence, mainly for neutrally buoyant and heavy particles. As we discuss in this review, for a variety of reasons, heavy and neutrally buoyant particle–laden flows are experimentally, numerically, and theoretically more tractable than their bubble-laden counterparts (14).

Balachandar & Eaton (15) recently reviewed important aspects of turbulent bubbly flows. However, they do not consider how the buoyancy of gas bubbles and light particles can manifest in various forms in turbulent multiphase settings. The aim of this review is to examine the subject from this perspective for bubbles and buoyant particles in turbulence. Therefore, all of the flows we consider are liquid, and henceforth we use the term buoyant particles generically to refer to both gas bubbles and light particles. Vapor bubbles, which have rich underlying physics of their own (16), are not discussed here.

The review is organized into several sections. We begin with the equations governing fluid motion and that of a particle suspended within the flow (Section 2). In Section 3, we address the dynamics of small bubbles and buoyant particles in a regime in which particle inertia is dominant, followed by a regime where buoyancy and inertia compete, leading to clustering and reduced rise velocities. We then explore the unsteady wake-induced dynamics of finite-sized buoyant particles and air bubbles, as well as their so-called lift and lateral migration tendencies. In Section 4, we discuss the main consequences of particle dynamics on flow modulations, including drag reduction and heat transfer enhancement pertaining to different turbulent flow systems. The review ends with a summary and outlook toward open issues for future research.

1.1. Dimensionless Groups

Covering the vast number of issues encountered in buoyant particle–laden turbulence would require an exhaustive compilation of the relevant dimensionless parameters (for a review of bubbles in general, see 14). In this review, we restrict our attention to a selected subset of these. We divide the control parameter space into particle parameters and flow parameters. For the bubble or buoyant particle, the following dimensionless groups are important: the density ratio of the particle (or bubble) to liquid, $\Gamma \equiv \rho_p/\rho_l$, and the size ratio, $\Xi \equiv d_p/l$, where d_p is the particle diameter and l is a characteristic length scale of the flow. By combining Γ and Ξ one can obtain the Stokes number, $St \equiv \tau_p/\tau_l$, where τ_p is the response time of the particle and τ_l is a characteristic timescale of the flow. We note that the problem is sufficiently defined once two of the three parameters

(Γ, Ξ, and St) are specified. Furthermore, one can include the effect of buoyancy (or gravity) by using two additional control parameters: the Froude number, Fr_{ug}, and the Galileo number, Ga. In the most general form,[1] $Fr_{ug} = U^2/(gd_p)$ gives the ratio of inertia to buoyancy, where U is a relevant velocity scale and g is gravitational acceleration. $Ga \equiv \sqrt{gd_p^3(\Gamma - 1)}/\nu$ compares buoyancy effects with viscous effects (17), where ν is the kinematic viscosity of the carrier liquid. Note that the above definition of the Galileo number, Ga, is alternatively referred to as the Archimedes number, Ar (18). Next, when the buoyant particle under consideration is a gas bubble, its deformability can have an influence on particle–turbulence interactions. The Eötvös number, $Eo = \rho_l gd_p^2/\sigma$ (also known as the Bond number, Bo), gives the ratio of buoyancy force to capillary force. Here, ρ_l is the liquid density and σ is the surface tension of the gas–liquid interface. Furthermore, when the buoyant particle's rotation is important, its mass moment of inertia ratio, $I^* \equiv I_p/I_l$ (where I_p is the particle moment of inertia and I_l is the moment of inertia of the displaced liquid), becomes a relevant control parameter. For turbulence, we refer to the Reynolds number, Re (with varying definitions based on the type of the turbulent flow), and the Rayleigh number, Ra (for thermal turbulence). With these parameters specified, we look at a variety of responses of the particles, as well as the flow modulations they induce.

Lastly, the volume fraction α of the dispersed phase is a crucial control parameter for the system. For particle-laden systems, it is common to specify a low–volume fraction threshold for transitions to two-way and four-way coupling regimes (13). For bubbly and light particle–laden turbulence, such a criterion is rarely used. As is often the case, even one buoyant bubble can significantly modify the turbulence around it. Thus, it is not appropriate to identify a threshold of bubble volume fraction below which bubbles can be considered passive. In this review, we restrict our discussion to situations of low and moderate volume fractions ($\alpha < 5\%$), where complex issues of coalescence and breakup (19) are not dominant.

1.2. Response Quantities

In addition to the abovementioned control parameters, we discuss the particle Reynolds number, $Re_p \equiv v_T d_p/\nu$, and the buoyancy parameter, $R_v \equiv v_T/u'$, which are estimable output parameters. Here, v_T is the measured mean particle rise velocity and u' is the root-mean-square velocity of the liquid fluctuations of single-phase turbulence. Broadly speaking, the Lagrangian dynamics of the particles and the various flow modifications they induce are the output quantities of importance. Our intention is to present these under one umbrella of familiar terminology. We provide further details of the dimensionless groups in the relevant sections of text.

2. PARTICLE MOTION IN A FLUID FLOW

The fluid motion in an incompressible multiphase flow is governed by the Navier–Stokes (NS) equations,

$$\frac{\partial \mathbf{U}}{\partial t} + (\mathbf{U} \cdot \nabla)\mathbf{U} = -\frac{\nabla p}{\rho_l} + \nu\nabla^2\mathbf{U} + \mathbf{f}_R, \qquad 1.$$

where $\mathbf{U}$ is the velocity at the location of the particle, p is the pressure, ρ_l is the liquid density, ν is the kinematic viscosity of the liquid, and $\mathbf{f}_R$ is a back-reaction force per unit mass on the fluid. On the basis of the flow setting and the modeling approach, $\mathbf{f}_R$ can be either exactly computed (11) or modeled (20, 21), or ignored altogether (7). Appropriate boundary conditions must be

---

[1]Note that many different, but equivalent, definitions of the Froude number are available.

applied on the boundaries of the fluid domain. For the particle, when employing fully resolved direct numerical simulations (DNS), the boundary condition is either no slip or free slip, or a combination of the two.

We begin by considering the equation of motion of a small buoyant spherical particle advected in a fluid flow with velocity $\mathbf{U}[\mathbf{X}(t), t]$, and in the presence of gravity. Assuming the particle's spatial dimension is pointlike, one can use a form of equation in the spirit of the celebrated Maxey–Riley equation (22):

$$\mathcal{V}_\mathrm{p} \, \rho_\mathrm{p} \, \ddot{\mathbf{X}}_\mathrm{p} = \mathcal{V}_\mathrm{p} \, \rho_\mathrm{l} \frac{\mathrm{D}\mathbf{U}}{\mathrm{D}t} + \mathbf{F}_\mathrm{M} + \mathbf{F}_\mathrm{B} + \mathbf{F}_\mathrm{L} + \mathbf{F}_\mathrm{D}, \qquad 2.$$

where $\mathbf{X}_\mathrm{p}$ is the position of the particle (or bubble); $\mathcal{V}_\mathrm{p} = (\pi d_\mathrm{p}^3)/6$ is its volume; and ρ_l and ρ_p are the liquid and particle mass densities, respectively. In obtaining the above equation, we have assumed that the coupling between translation and rotation of the particle is negligible. The forces contributing on the right-hand side, other than those due to the accelerated flow (which includes the pressure gradient term), are the added mass $\mathbf{F}_\mathrm{M}$, drag $\mathbf{F}_\mathrm{D}$, buoyancy $\mathbf{F}_\mathrm{B}$, and a so-called (shear-induced) lift $\mathbf{F}_\mathrm{L}$. Generally, they are modeled as

$$\mathbf{F}_\mathrm{M} = C_\mathrm{M} \rho_\mathrm{l} \mathcal{V}_\mathrm{p} \left(\frac{\mathrm{D}\mathbf{U}}{\mathrm{D}t} - \ddot{\mathbf{X}}_\mathrm{p} \right), \qquad 3.$$

$$\mathbf{F}_\mathrm{B} = \mathcal{V}_\mathrm{p} \, (\rho_\mathrm{p} - \rho_\mathrm{l}) \, g \, \hat{\mathbf{e}}_y, \qquad 4.$$

$$\mathbf{F}_\mathrm{L} = -C_\mathrm{L} \rho_\mathrm{l} \mathcal{V}_\mathrm{p} (\dot{\mathbf{X}}_\mathrm{p} - \mathbf{U}) \times (\nabla \times \mathbf{U}), \qquad 5.$$

$$\mathbf{F}_\mathrm{D} = -C_\mathrm{D} \frac{\pi d_\mathrm{p}^2}{8} \rho_\mathrm{l} |\dot{\mathbf{X}}_\mathrm{p} - \mathbf{U}| (\dot{\mathbf{X}}_\mathrm{p} - \mathbf{U}), \qquad 6.$$

where C_M is the added mass coefficient and g is the gravitational acceleration directed along $\hat{\mathbf{e}}_y$, the unit vector in the vertical direction. The shear-induced lift depends on the alignment between the vorticity vector ($\nabla \times \mathbf{U}$) and the relative velocity of the particle ($\dot{\mathbf{X}}_\mathrm{p} - \mathbf{U}$), and C_L and C_D are the constants of proportionality for lift and drag, respectively (i.e., lift and drag coefficients). It is important to first appreciate the directions of these force vectors for a rising buoyant particle. **Figure 1a** presents a simplified picture of a buoyant particle rising along the downward side of a vortex. Note that the Faxén forces (accounting for flow nonuniformity at the particle scale) and the Basset history force are omitted for simplicity (24, 25). The relative importance of these terms for buoyant rising particles is still to be resolved (26–28).

When the condition of the particle's Reynolds number, $\mathrm{Re}_\mathrm{p} \ll 1$, is met, the drag coefficient reduces to $C_\mathrm{D} = 24/\mathrm{Re}_\mathrm{p}$, which implies the following linear drag relation: $\mathbf{F}_\mathrm{D} = -3\pi \mu d_\mathrm{p} (\dot{\mathbf{X}}_\mathrm{p} - \mathbf{U})$. While the basic form of this equation is founded on a unified treatment of particles, drops, and bubbles, it also assumes that, for $\mathrm{Re}_\mathrm{p} \ll 1$, the particle locally sees a Stokes flow (22, 29) despite the unsteadiness and turbulence of the carrier flow. The expression for drag used above assumes a contaminated air–liquid interface for the bubble. For a clean bubble interface, the prefactor of $\mathbf{F}_D$ is slightly modified (30), although it retains its functional form. The assumption of a contaminated interface is indeed reasonable for most natural and industrial flows, since the carrier liquid is almost never ultrapure. Assuming potential flow in the outer regions, we can use $C_\mathrm{M} = 1/2$. Similarly, by considering the momentum flux far from the particle, one can obtain the Auton lift, $C_\mathrm{L} = 1/2$ (24, 31), which applies to small spherical bubbles or particles in a shear flow.

For the purpose of simplification, we now consider the turbulence to be homogeneous and isotropic. A state of homogeneous isotropic turbulence (HIT) is fully determined by knowing
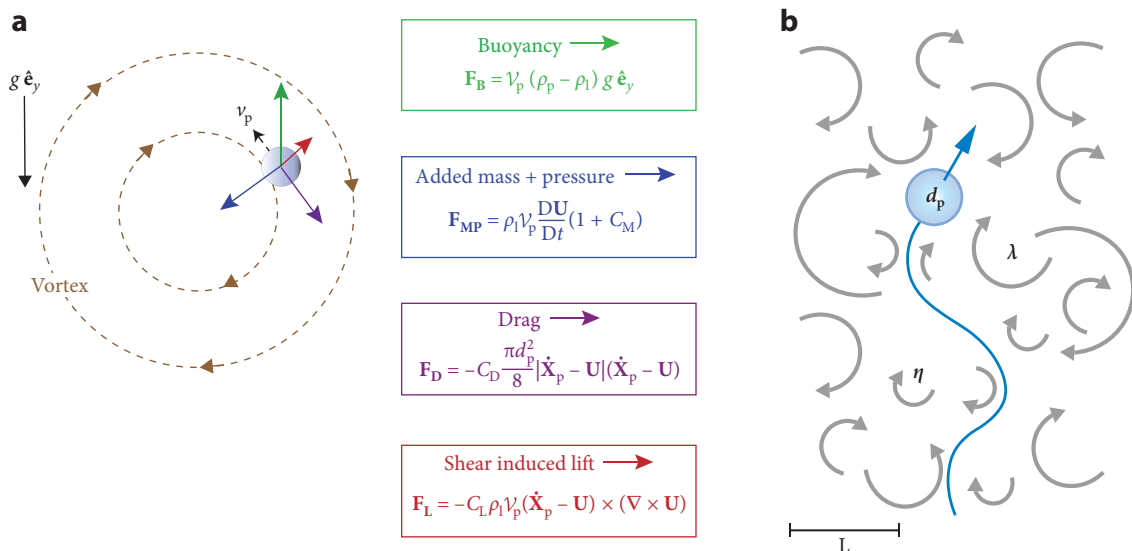
a

$g\,\hat{\mathbf{e}}_y$

v_p

Vortex

Buoyancy
$$\mathbf{F}_\mathrm{B} = \mathcal{V}_\mathrm{p}\,(\rho_\mathrm{p} - \rho_\mathrm{l})\,g\,\hat{\mathbf{e}}_y$$

Added mass + pressure
$$\mathbf{F}_\mathrm{MP} = \rho_\mathrm{l}\mathcal{V}_\mathrm{p}\frac{\mathrm{D}\mathbf{U}}{\mathrm{D}t}(1 + C_\mathrm{M})$$

Drag
$$\mathbf{F}_\mathrm{D} = -C_\mathrm{D}\frac{\pi d_\mathrm{p}^2}{8}|\dot{\mathbf{X}}_\mathrm{p} - \mathbf{U}|(\dot{\mathbf{X}}_\mathrm{p} - \mathbf{U})$$

Shear induced lift
$$\mathbf{F}_\mathrm{L} = -C_\mathrm{L}\rho_\mathrm{l}\mathcal{V}_\mathrm{p}(\dot{\mathbf{X}}_\mathrm{p} - \mathbf{U}) \times (\nabla \times \mathbf{U})$$

b

d_P

λ

η

L

Figure 1

A buoyant spherical particle in a turbulent flow. (*a*) Forces (represented as point forces) felt by a small buoyant particle or gas bubble rising past a vortex (a simplified representation of turbulent eddy). v_p is the instantaneous particle velocity vector, and the forces due to buoyancy ($\mathbf{F}_\mathrm{B}$), drag ($\mathbf{F}_\mathrm{D}$), so-called lift ($\mathbf{F}_\mathrm{L}$), and the net effect of added mass and pressure ($\mathbf{F}_\mathrm{MP}$) are represented by colored arrows giving their relative directions. The drag (*purple arrow*) is oriented to oppose the direction of the particle's velocity; the buoyancy (*green arrow*) is vertical; and the shear-induced lift force (*red arrow*) acts perpendicularly to the plane containing the particle velocity and the vorticity vector and is opposed by the centrifugal force (*blue arrow*) that is directed toward the eye of the vortex, as the particle is lighter than the surrounding liquid. $\mathbf{F}_\mathrm{MP}$ is obtained by rearranging the added mass and fluid force terms in Equation 2, and it accounts for the pressure force on the buoyant particle. For details of the variables shown, see Equations 3–6. (*b*) The buoyant particle rising through a turbulent flow composed of vortices (or eddies) of various length and timescales. d_p is the particle diameter, η is the dissipative length scale, and L is the integral length scale of the flow (7, 23). λ is an intermediate length scale, commonly known as the Taylor microscale.

the kinematic viscosity ν, an outer length scale, and a timescale. A bubble or light particle rising through HIT (**Figure 1b**) sees the largest and smallest length scales, which are the energy injection scale L and the Kolmogorov (or dissipative) scale η, respectively. Additionally, λ represents an intermediate scale known as the Taylor microscale, upon which the Taylor–Reynolds number, $\mathrm{Re}_\lambda \equiv u'\lambda/\nu$, is based. Since the particle size is comparable to the dissipative scale, it is appropriate to nondimensionalize the equation of particle motion by using the Kolmogorov units of length (η) and time (τ_η). This leads to

$$\ddot{\mathbf{x}}_\mathrm{p} = \beta\frac{\mathrm{D}\mathbf{u}}{\mathrm{D}t} + \frac{1}{\mathrm{St}}(\mathbf{u} - \dot{\mathbf{x}}_\mathrm{p}) + \frac{1}{\mathrm{Fr}}\hat{\mathbf{e}}_y + \frac{\beta}{3}(\mathbf{u} - \dot{\mathbf{x}}_\mathrm{p}) \times \boldsymbol{\omega}, \qquad 7.$$

where the lowercase bold variables $\mathbf{x}_\mathrm{p}$, $\mathbf{u}$, and $\boldsymbol{\omega}$ denote the new dimensionless vectors for particle position, flow velocity, and vorticity, respectively. $\beta \equiv 3/(1 + 2\Gamma)$ is an effective density ratio that takes the fluid added mass into account. The Stokes number, $\mathrm{St} \equiv d_\mathrm{p}^2/12\beta\nu\tau_\eta$, and the Froude number, $\mathrm{Fr} \equiv a_\eta/[(\beta - 1)g]$, are defined generically to be valid for light ($1 < \beta \le 3$), heavy ($0 \le \beta < 1$), and neutrally buoyant ($\beta = 1$) particles. $a_\eta \equiv \eta/\tau_\eta^2$ is the acceleration at the Kolmogorov scale.
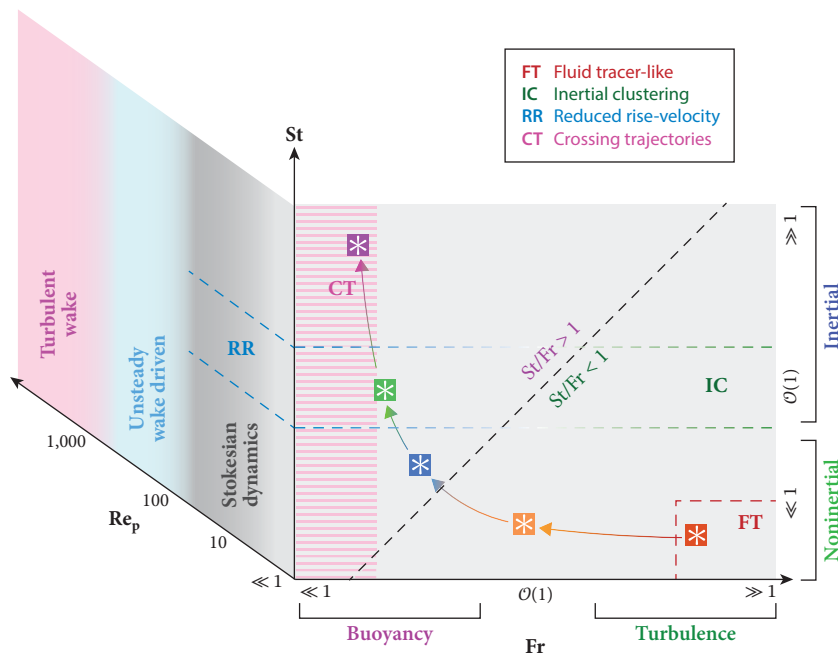
Figure 2

A simplified regime diagram for a buoyant particle or air bubble in a turbulent flow. The dynamics of the particle can be summarized as a function of three dimensionless parameters: the Stokes number (St), a measure of particle inertia; the Froude number (Fr), the ratio between turbulence strength and gravity; and the particle Reynolds number (Re_p) (27, 32). The different regimes are **FT** (fluid tracer–like), **IC** (inertial clustering), **RR** (reduced rise velocity), and **CT** (crossing trajectories). The horizontally hatched (*magenta*) region is the regime where the effect of crossing trajectories can be observed to various extents, depending on the value of St. The asterisks (*connected by arrows*) help illustrate a gradual regime transition seen by an air bubble (density ratio $\Gamma = 10^{-3}$) upon increasing its size at constant turbulence level, and assuming that $Re_p \ll 1$. Note that the figure does not capture the effects of changing Γ and size ratio (Ξ).

3. BUOYANT PARTICLE DYNAMICS

3.1. Regimes of Dynamics

A wealth of intriguing phenomena have been reported for buoyant particle suspensions in turbulent flows. **Figure 2** depicts a simplified regime diagram for a buoyant spherical particle (or bubble) when the particle parameters St, Fr, and Re_p are varied, with Γ, Ξ, and background turbulent flow unchanged. When extremely small, bubbles (or light particles) can serve as a passive flow visualization tool (33), while in other scenarios, they have been used to selectively sample intense vortical structures present in flows (33, 34). It is widely known that in the case of finite particle inertia [St $\sim \mathcal{O}(1)$ and Fr $\gg 1$] bubbles cluster in high-vorticity regions (**Figure 2**). Several researchers (20, 35, 36) observed these effects in their simulations of HIT laden with microbubbles. The phenomenon was later extensively explored by others (37, 38), thus providing a unified understanding of the clustering behavior of light, heavy, and neutrally buoyant particles. The methods adopted to quantify clustering have been diverse, with some (37) using the Kaplan–Yorke dimension and Minkowski functionals and others (39–42) using Voronoï tessellations or simply the relative particle concentration in high-vorticity regions (21), but all to the same end. An assessment of the actual forces that bubbles are subjected to in turbulent environments was performed by Volk et al.

(43, 44), who experimentally investigated the acceleration dynamics of small bubbles ($d_p \approx 75$ μm) in a relatively intense turbulent flow ($Re_\lambda = 850$) generated by a von Kármán flow apparatus. The high intensity of turbulence ensured that the 75-μm air bubble had St =1.85 with Fr ∼10, which meant that the role of buoyancy was negligible. These bubbles showed an acceleration variance four times that of the fluid, presumably a combined effect of inertial forces and preferential accumulation in high-vorticity regions of the flow (27). For reviews of inertial particle dynamics in the absence of buoyancy, see References 7 and 8.

It is worthwhile to take a step back to appreciate the various regime transitions seen by an air bubble ($\Gamma = 10^{-3}$) when its size is increased with all other parameters kept fixed. Practically speaking, for a laboratory-scale turbulent water flow [say, $Re_\lambda \sim \mathcal{O}(100)$ and $L \sim 100$ mm], the actual regime transitions can be more complex. For instance, a microbubble with $d_p < 10$ μm can still be considered a good tracer of the turbulent flow, but when d_p is increased to around 100 μm, the effects of buoyancy begin to play a role in the dynamics. When the bubble is a few hundred micrometers in size, in addition to its buoyancy, the bubble's inertia becomes important, and when the diameter is increased further ($d_p > 500$ μm), one can expect noticeable non-Stokesian and finite-Re_p contributions. In the following sections, we discuss these regimes of dynamics in more detail.

3.2. Crossing Trajectories

This section addresses the dynamics of a particle advected in HIT in a regime where $Fr \equiv a_\eta/[(\beta - 1)g] < 1$. The importance of buoyancy ($Fr < 1$) naturally implies that the particle experiences a mean vertical drift through the turbulent flow, hence the term crossing trajectories (**Figure 1b**).

3.2.1. Noninertial particles with buoyancy.
We begin with bubbles and buoyant particles that are in the noninertial limit, that is, with St ≪ 1. Since a very small St naturally implies tiny particle dimensions, such bubbles are commonly used as tracers in turbulence experiments. Recently, Mathai et al. (32) conducted a combined experimental and numerical study of the dynamics of such small bubbles and particles in the noninertial (St ≪ 1) limit. An interesting consequence of buoyancy is that even low-St bubbles are subject to intense acceleration. For Fr ≪1 and St ≪1, Equation 1 is dictated by the balance between only the drag and buoyancy terms, yielding the expression $\ddot{\mathbf{x}}_p \simeq D\mathbf{u}/Dt + (St/Fr)\partial_y\mathbf{u}$, where $\partial_y\mathbf{u}$ are the gradients of the turbulent flow velocity at the particle's location. The buoyancy parameter can be exactly computed as $R_v = u_\eta St/(u'Fr)$. The acceleration variance (*i*th component) of the buoyant particle $\langle a_p^2 \rangle_i$ can be expressed as an enhancement over the fluid acceleration variance $\langle a_f^2 \rangle$:

$$\frac{\langle a_p^2 \rangle_i}{\langle a_f^2 \rangle} \simeq 1 + \kappa_i \left(\frac{St}{Fr}\right)^2, \qquad\qquad 8.$$

where $\kappa_x = 2/(15a_0)$ for the horizontal component and $\kappa_y = 1/(15a_0)$ for the vertical component, with a_0 the so-called Heisenberg–Yaglom constant (45). These relations follow exactly from the assumption that the turbulence is statistically isotropic (23). In other words, the increase in acceleration variance is a direct consequence of the vertical drift of the bubble through the turbulent eddies. While the acceleration variance increases, its decorrelation time compared with the fluid is suppressed (**Figure 3a,b**), as the drifting particle spends comparatively less time within the turbulent eddies. Similarly, the kurtosis of acceleration is diminished because the spatial velocity gradients $\partial_y\mathbf{u}$ in turbulence are less intermittent than the fluid acceleration (for further details, see 32). Finally, we note that in this noninertial limit the behavior of buoyant particles is expected to be nearly identical to that of heavy particles, for fixed St/Fr (46–48). Of course, the effect is
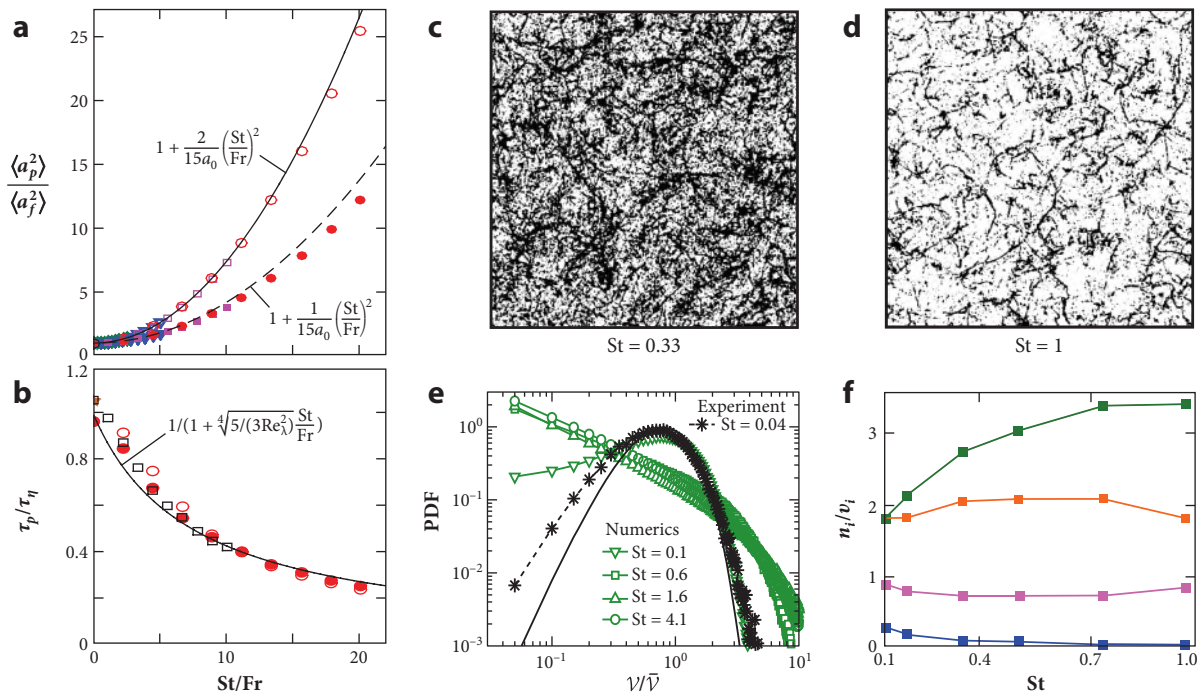
Figure 3

Accelerations and clustering behavior of small ($\Xi < 1$) buoyant particles and bubbles in isotropic turbulence obtained using
Euler–Lagrangian direct numerical simulations (DNS) with the inclusion of buoyancy and lift. (*a*) Normalized acceleration variance of
buoyant noninertial (St $\ll$ 1) particles in turbulence versus St/Fr at $Re_\lambda = 75$. The acceleration variance here is normalized by the
acceleration variance of the fluid. (*b*) Normalized acceleration decorrelation time (time to reach an autocorrelation value of 0.5) of the
particles for the same cases as in panel *a*. The normalization here is with the Kolmogorov timescale of the turbulence. In panels *a* and *b*,
solid and hollow symbols correspond to vertical (gravity direction) and horizontal components, respectively. The solid and dashed
curves represent theoretical predictions. (*c,d*) Projections of bubble distribution in isotropic turbulence ($Re_\lambda = 62$) for St = 0.33 and
St = 1. Note that the particle concentration is identical for both panels. Bubble clustering is pronounced in the St = 1 case (*d*). We
estimate the ratio St/Fr ($\approx v_T/u_\eta$) to be 1.0 and 3.0 in panels *c* and *d*, respectively, implying $R_v < 1$. (*e*) Clustering of light particles in
turbulence, quantified using probability density functions (PDFs) of normalized Voronoï volumes for different values of St. The solid
curve is a Gamma distribution, which is representative for nonclustering (randomly distributed) particles. Green data points are based
on DNS using an Euler–Lagrangian (point–particle) model, at $Re_\lambda = 180$. Black data points represent experimental data for
microbubbles (St = 0.04) in turbulence at $Re_\lambda = 162$. The results suggest that maximum clustering for bubbles occurs at St around 1–2.
(*f*) Number of bubbles located in a particular zone of fluid, n_i, normalized by the volume fraction of that zone, v_i, versus St. Here,
again, $Re_\lambda = 62$, and St/Fr is kept fixed at 1. The symbol colors refer to zones: eddy (*green*), shear (*orange*), streaming (*magenta*), and
convergence (*blue*). Panels *a* and *b* adapted from Reference 32. Panels *c* and *d* adapted from Reference 20. Panel *e* adapted from
Reference 40. Panel *f* adapted from Reference 21.

more pronounced for bubbles because their density contrast is generally larger than that of heavy
particles in liquid flows. Thus, a tiny bubble or droplet is not necessarily a good tracer of turbulent
acceleration. In reality, the situation of finite g/a_η is common for bubbles that drift through the
oceans ($g/a_\eta \approx 100$–1,000) and for droplets settling through clouds ($g/a_\eta \approx 10$–100) (49). On the
practical side, these also point to the key condition St/Fr $\ll$ 1 that must be met (in addition to
St $\ll$ 1) for the usage of small bubbles (or droplets) in flow visualization and particle tracking in
turbulent flows.

3.2.2. Inertia and buoyancy. Next, we consider the cases when Fr $\leq$ 1 and St $\sim$ 1, that is,
a regime in which both buoyancy and inertia are important and in competition. Employing an

Euler–Lagrangian point–particle (PP) approach of a form similar to Equation 7, Mazzitelli et al. (20) studied the effect of increasing St at fixed Fr for bubbles rising in isotropic turbulence ($Re_\lambda = 62$). **Figure 3c,d** depicts the bubble distribution obtained from their simulations. At St = 0.33, the particles (bubbles) are nearly uniformly distributed, but at St = 1, clustering is visibly amplified. A three-dimensional Voronoï analysis was used to quantify the clustering of bubbles in HIT turbulence by use of data sets from numerics in the PP limit (without gravity and lift) and experimental data (40). For bubbles, Tagawa et al. (40) observed that the probability of finding both small and large Voronoï volumes $\mathcal{V}/\overline{\mathcal{V}}$ is generally higher. The two regions of small and large volumes can be used to identify clusters and voids. A high probability for low values of $\mathcal{V}/\overline{\mathcal{V}}$ signifies intense clustering. As shown in **Figure 3e**, when St increases, the probability of finding clusters (and voids) increases and reaches a maximum around St ≈ 1.6, suggesting that the strongest clustering for bubbles occurs in the St range of 1–2. A direct quantification of the clustering in the presence of buoyancy is shown in **Figure 3f**. Since the buoyancy and lift terms were included in Reference 21, the relative degree of clustering is typically less than what is observed in the minimalistic simulations presented in Reference 38, where these terms were neglected.

3.2.3. Non-Stokesian bubbles and particles.

For the more common situation of air bubbles in water flows, an St of order 1 typically almost never satisfies the condition of $Re_p \ll 1$ (50, 51). Therefore, a modified consideration of the drag, added mass, and lift forces is essential to predict the trajectory of finite-sized and finite-Re_p bubbles. As a model problem, Sridhar & Katz (52) experimentally studied the entrainment of such air bubbles ($d_p \approx 500$–$800\ \mu m$) by a vortex ring. They reported that the drag coefficient was comparable to the Schiller–Naumann parameterization (**Figure 4a**), while the lift forces did not agree with the existing theoretical or numerical models (22, 47, 53). More recently, Aliseda & Lasheras (54) experimentally investigated the behavior of small spherical bubbles ($d_p \approx 100$–$1,000\ \mu m$) immersed in a homogeneous isotropic
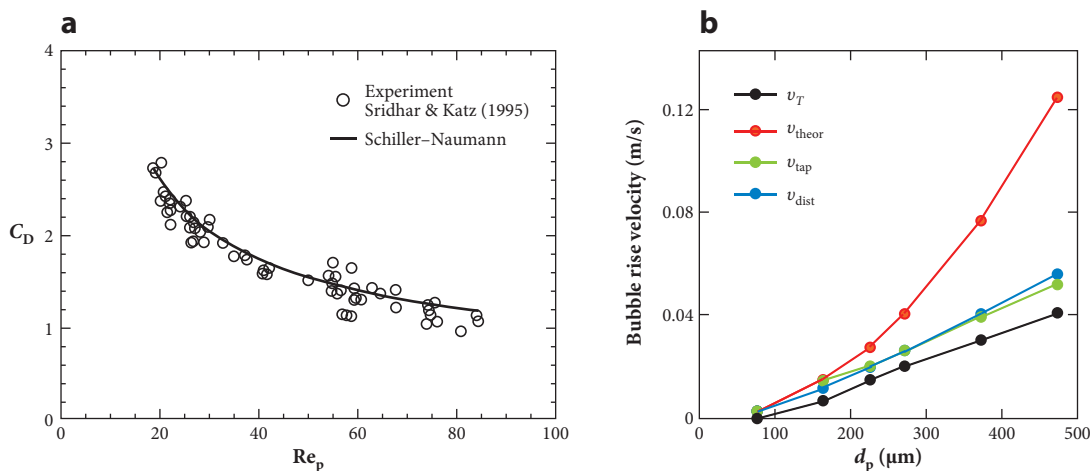

Figure 4

Drag coefficient and rise velocity modifications for submillimetric air bubbles rising in turbulent flows. (*a*) Comparison of the drag coefficient for 500–800-μm-diameter air bubbles (in a vortical flow), along with the predictions of the Schiller–Naumann drag model. (*b*) Direct measurements of rise velocity v_T for small bubbles versus bubble diameter d_p in a grid-generated turbulent flow at $Re_\lambda \approx 404$ (as roughly estimated by us). For comparison, v_{theor} is the terminal velocity estimated theoretically using Stokes drag $C_D = 24/Re_p$, v_{dist} is the terminal velocity measured in triply distilled water, and v_{tap} is the same quantity measured for tap water. Data in panel *a* adapted from Reference 52. Data in panel *b* adapted from Reference 54.

turbulent water flow (**Figure 4b**). Within the turbulent flow, the concentration field of the bubbles was altered, with preferential accumulation at the smaller scales and reduced rise velocities in comparison to the value in stationary liquid. These effects were interpreted as occurring due to two phenomena. First, the pressure fluctuations drive the inertial bubbles to the cores of the vortices. Second, the lift forces cause the bubbles to be preferentially transported toward downflow regions, where, in combination with an increased relative velocity (increased viscous drag), they are further slowed down (**Figure 1a**) (21).

The conditions of small size ($d_p/\eta \leq 1$) and nearly spherical shape are typically satisfied only for submillimetric air bubbles (52, 54). However, most bubble-laden turbulence operates under conditions where the bubbles are of finite size, free to move, and, most importantly, deformable (55, 56). These call for a more detailed consideration of the coupled interaction between the bubble topology and its wake-induced dynamics arising from the finite-Re_p and finite–Weber number (We) effects (57). A fully resolved treatment of the interaction between isotropic turbulence and large solid spherical particles has been performed in a variety of configurations (28, 58, 59). In comparison, DNS of turbulent bubbly flows are challenging because of the interface deformations and internal circulations, along with the need to resolve a wide range of length and timescales inherent to the turbulent flow. Loisy & Naso (60) used DNS to study an isolated deformable bubble freely rising in an otherwise isotropic turbulent flow (**Figure 5a**). Both the buoyancy parameter ($R_v \in$ [0.63, 2.17]) and the bubble Reynolds number ($Re_p \in [17, 62]$) are moderate; therefore, in quiescent liquid such bubbles rise along straight vertical paths. However, with decreasing R_v the trajectories become erratic and increasingly deviate from vertical paths (**Figure 5b–d**), accompanied by a reduction in rise velocities. With regard to the statistics of bubble velocity and acceleration, the probability distribution functions (PDFs) were nearly Gaussian for the velocity and showed stretched tails for accelerations. Lastly, the bubble showed a preference for increased residence in vorticity-dominated regions, computed here using the discriminant $D = 27R^2 + 4Q^3$, where Q and R are the second and third invariants of the velocity gradient tensor, respectively (61). This result was determined by conditional sampling of the average discriminant profile and discriminant field around the bubble (see **Figure 5e** and **h**, respectively).

The above analyses (60) show that the dynamics of moderate-Re_p bubbles in turbulence (rise velocity, PDF shapes, and clustering) are at least qualitatively captured by the PP model (27) despite their finite Re_p, finite size, and deformed shape. However, this does not reflect the full picture, since certain aspects of the bubble statistics are markedly different from the PP predictions. The PDF of the longitudinal acceleration, namely the component of bubble acceleration directed along its instantaneous velocity, was found to be negatively skewed, a feature not captured by the PP model even with the inclusion of a back-reaction force. It remains to be determined whether the origin of the negative skew actually lies in the time irreversibility (62) of turbulence, as postulated by Loisy & Naso (60), or in the asymmetry of flow-induced forcing on the bubble.

3.3. Wake-Driven Dynamics and Path Instabilities

With increasing buoyancy over inertia, the bubble or buoyant particle's Re_p can reach a few hundred. Two important changes come into effect in this regime. First, the mean drag coefficient loses its Reynolds number dependence, and C_D becomes weakly dependent on Re_p. Second, such bubbles and particles experience fluctuating components of forces that originate from the instability of their wakes. Although the mean forces on the particle can still be approximated, the instantaneous drag and lift can no longer be described using simplified coefficients. Furthermore, owing to the lightness of the particle, this regime paves the way for a strong coupling between the unsteady wake dynamics and particle motion, often resulting in vigorous path instabilities (18, 63–67). As
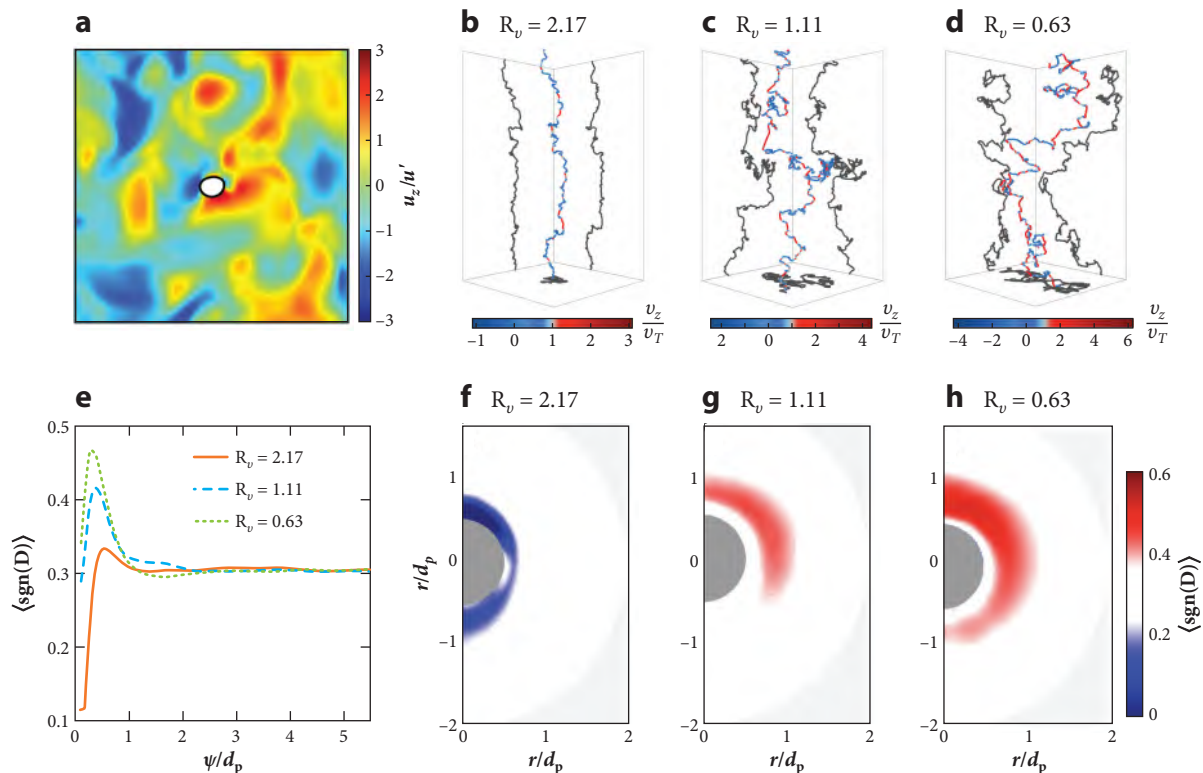
Figure 5

Direct numerical simulations of a slightly deformed bubble ($\Xi \approx 10$; $Re_p \in [17, 62]$) rising in a turbulent flow at $Re_\lambda = 30$. (*a*) Snapshot of the (normalized) vertical velocity field of the turbulent flow on a plane passing through the bubble center. (*b–d*) Sample bubble trajectories for decreasing buoyancy parameter $R_v \equiv v_T/u'$: (*b*) $R_v = 2.17$, (*c*) 1.11, and (*d*) 0.63. The bubble trajectories are colored by their instantaneous vertical velocity normalized by their terminal velocity. (*e*) Radially averaged profile of discriminant D around the bubble for the three different R_v cases. The abscissa ψ/d_p is the (normalized) radial distance from the centroid of the bubble. The sign of the discriminant D (ordinate) can be used to highlight the vorticity-dominated regions. (*f–h*) Average discriminant field around the bubble for decreasing R_v (*left to right*). The color scale is centered around the mean value $\overline{D} \approx 3$ to show that values above $\overline{D}$ are the vorticity-dominated regions. The discriminant field clearly demonstrates that clustering in high-vorticity regions increases as the bubble rise velocity decreases. Figure adapted from Reference 60.

reported by Risso (68), there is now compelling evidence that the wakes and dynamics of isolated buoyant particles are remarkably robust to turbulent perturbations (69). Therefore, the forces acting on an isolated buoyant particle in a flow can still provide a basis for understanding dispersed two-phase flows.

3.3.1. Wake-driven bubbles. Building on the original formulations proposed by Kirchhoff for a rigid particle in an arbitrary irrotational flow (70, 71), Mougin & Magnaudet (30) extended this case to a situation where the NS equations governing the liquid flow (72, 73) are considered in conjunction with Newton's laws for the translational and rotational dynamics of a fixed-in-shape nonspherical bubble or buoyant particle. The Kelvin–Kirchhoff equations, which disregard small-scale deformability effects, demonstrate that wake instability and anisotropic added-mass effects of oblate spheroids (63, 74) are indeed sufficient to explain the experimentally observed path instabilities (75) of millimetric bubbles. This method, now readily available, has yet to be used
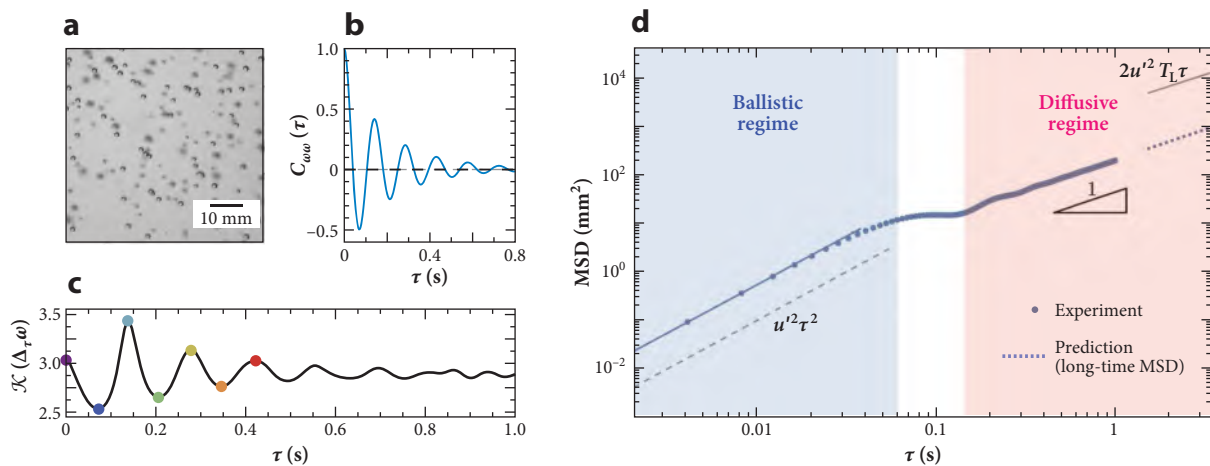
Figure 6

The horizontal component of velocity and dispersion for 1.8-mm-diameter air bubbles ($R_v \approx 10$) rising in active-grid-generated turbulence at $Re_\lambda = 110$. Here, the bubble size ratio $\Xi \approx 5$. (*a*) A sample image from one of the cameras. (*b*) Lagrangian temporal autocorrelation function of the horizontal component of the bubble velocity. (*c*) Kurtosis of the horizontal velocity–increment probability distribution function as a function of time lag τ. (*d*) Horizontal component of the mean-squared displacement (MSD) for the bubble as a function of time lag τ. The well-known ballistic–diffusive behavior of fluid tracers is shown for comparison: The dashed gray line represents $\propto \tau^2$, and the solid gray line represents $\propto 2T_L\tau$. The dotted blue line on the right shows the prediction for the reduced long-time dispersion for the bubble, obtained using the crossing-trajectories hypothesis. Figure adapted from Reference 51.

widely for turbulent bubbly flows, and it holds the potential to yield useful insights at a reduced computational cost, since the condition of a continuously deforming bubble interface is relaxed.

Mathai et al. (51) have experimentally studied the dynamics of isolated millimetric air bubbles in turbulent flows. These authors generated a suspension of air bubbles ($d_p \approx 1.8$ mm) in active-grid turbulence with $Re_\lambda \in [110, 300]$. The bubbles were nearly spherical (**Figure 6a**), and their volume fraction in the experiments was low ($\alpha \sim 5 \times 10^{-4}$). At a low level of turbulence ($Re_\lambda = 110$), both the Lagrangian temporal autocorrelation of the bubble velocity and its kurtosis showed periodicity (**Figure 6b,c**), which clearly indicated wake shedding at a frequency $f_{viv} \sim 0.1 v_p/d_p$. The effects of these on the spreading of the bubbles was analyzed using mean-squared displacement (MSD), which was then compared with the well-known regimes of Taylor dispersion for the fluid in turbulence (**Figure 6d**). At short times, the bubble MSD grows ballistically ($\propto \tau^2$), whereas at a longer timescale set by the wake-shedding frequency f_{viv}, it approaches the diffusive regime, where MSD $\propto \tau$. Note that the ballistic regime of the bubbles lies well above the $u'^2\tau^2$ prediction of fluid tracers, whereas the diffusive regime of the bubbles lies well below the $2u'^2 T_L\tau$ prediction of fluid tracers (here, T_L is the Lagrangian integral timescale, which sets the ballistic–diffusive transition time for fluid tracers in turbulence). Thus, with high–Reynolds number millimetric air bubbles in turbulence, we can appreciate an elegant merger of two classical phenomena: the wake-induced velocity fluctuations of the bubbles (at short times) and the reduced dispersion (at longer times) originating from the crossing-trajectories effect (2, 32, 51, 76).

Ravelet et al. (77) have studied the motion of an even larger bubble ($d_p \approx 9$ mm) in turbulence. At these sizes in a turbulent water flow, the bubble shows considerable deformability (We $\simeq 11.6$), and its Reynolds number, $Re_p \approx 2,800$. These researchers tracked the bubble motion and orientation in intricate detail using three-dimensional shape recognition, yielding statistics of bubble translation, rotation, and deformation in turbulence (**Figure 7a–d**). The bubble dynamics was
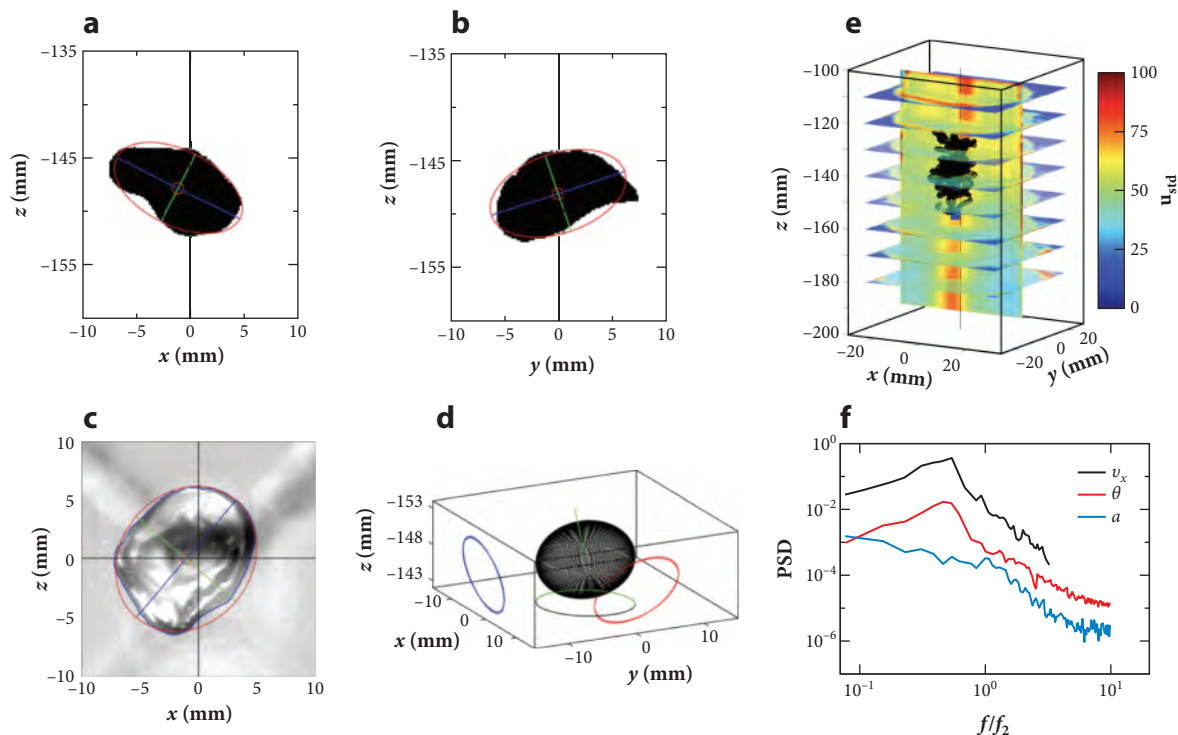
Figure 7

Kinematics of a deformable air bubble ($d_p \approx 9.3$ mm; $Re_p = 2{,}800$) rising in a (rotating) grid-generated turbulent flow (77). The buoyancy parameter R_v lies in the range [5, 10]. (*a–d*) Image-processing steps on the bubble images, with equivalent ellipse (*red*), center of mass (*red circle*), major axis (*blue*), and minor axis (*green*) of the best-fit ellipsoid. (*e*) Standard deviation of the liquid velocity measured in one vertical plane and eight horizontal planes, superimposed on a trajectory of the bubble (*black*). Note that the bubble is trapped in a region of highest vorticity. (*f*) Normalized power spectral density (PSD) of horizontal velocity v_x (*black*), orientation θ (*red*), and major axis a (*blue*). The spectra are normalized by the frequency $f_2 = 15$ Hz, as in Reference 77.

found to be governed by three fairly independent mechanisms. First, the average bubble shape is imposed by the mean motion of the bubble relative to the liquid. Second, the wake instability of the bubble generates periodic oscillations in its velocity and orientation. Third, the turbulence adds to the random deformations, which under rare circumstances can even lead to bubble breakup. Such bubbles were observed to be trapped inside a vortex at the core of the flow (**Figure 7e**). The temporal spectra of horizontal velocity, orientation, and semiaxis lengths (**Figure 7f**) reveal peaks at around 8.5 Hz. This is consistent with wake instability and yields a Strouhal number (Sr) of ∼0.27.

3.3.2. Wake-driven rigid buoyant particles. In the following discussion, we provide an overview of studies on large buoyant particles of fixed shape advected in turbulent flows. Initial progress was made using finite-sized neutrally buoyant spherical particles (78–80). From a modeling perspective, the PP approach with the so-called Faxén corrections (22, 81) for particle size was widely adopted for the study of neutrally buoyant spherical particles (27). Still, the question of finite-slip velocities, which occur in most practical situations, raises important concerns about the validity of this treatment (12). By performing experiments using marginally buoyant ($\beta \approx 1.05$) rigid finite-sized spheres in turbulence, Mathai et al. (82) showed that even a slight density mismatch is sufficient to cause the dynamics of buoyant particles to deviate significantly
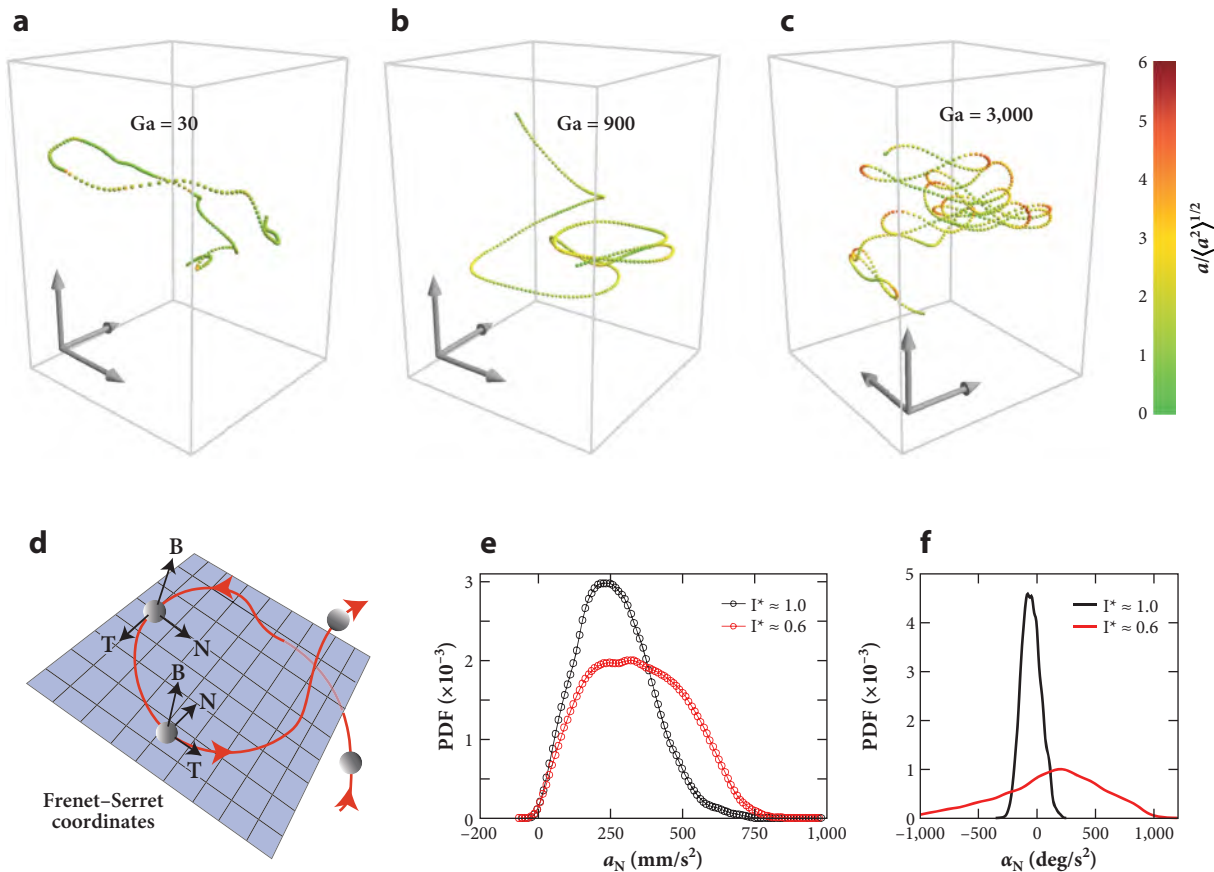
Figure 8

Kinematics and dynamics of rigid buoyant spheres ($\Xi \approx 10$) in a turbulent flow with $Re_\lambda \approx 300$. (*a–c*) Three-dimensional trajectories of buoyant spheres for increasing Galileo number (Ga). In obtaining these trajectories, the mean rising motion of the spheres was counteracted by matching the sphere rise velocity with the mean downward flow speed. Note that the increase in Ga coincides with an increase in the buoyancy parameter $R_v \equiv (v_T/u')$, which was measured to be around (*a*) 1.7, (*b*) 13.6, and (*c*) 45.6. (*d*) The Frenet–Serret coordinates [tangent (**T**), normal (**N**), and binormal (**B**)] were used to decompose the instantaneous motion of the sphere in turbulence. (*e*) Probability distribution functions (PDFs) of the centripetal acceleration a_N for two spheres with identical properties ($\Gamma = 0.89$; $\Xi \approx 100$; Ga = 6,000), except their mass moments of inertia, $I^* = 1.0$ (*black circles*) and 0.6 (*red circles*). Here, a_N is directed along the **N** vector in the Frenet–Serret formulae. Reducing I^* triggers a dramatic increase in the (*e*) translational and (*f*) rotational accelerations. Panels *a–c* adapted from Reference 82. Panels *d–f* adapted from Reference 65.

from the Faxén model predictions. The deviations increase dramatically upon reducing the density ratio until, for very buoyant particles with $\beta \approx 2.90$ (i.e., comparable to the β of a bubble), vigorous path oscillations outweigh the turbulence-induced motion. **Figure 8*a–c*** demonstrates this effect of increasing buoyancy (Ga = 30–3,000): The turbulence-induced chaotic dynamics in panel *a* are replaced by wake-induced oscillations in panels *b* and *c*, reminiscent of Lissajous orbits (83).

Three mechanisms contribute to the increasing path oscillations observed here. First, an increase in Ga strengthens the wake-induced forces. Second, there is an accompanying increase in the buoyancy parameter, $R_v \equiv v_T/u'$. When R_v increases, the rising spherical particle crosses the turbulent eddies at increasingly high speeds, thus having little time to respond to the turbulent fluctuations. A third, not so obvious, influence was revealed experimentally in a recent study (65),

which hints that the observed path instabilities are also augmented by the particle's rotational motions. To explain this finding, we revisit the Kelvin–Kirchhoff equations expressing linear and angular momentum conservation for a buoyant spherical particle:

$$\left(\Gamma + \frac{1}{2} + B_1\,\delta\right)\frac{d\mathbf{V}_p}{dt} + \Gamma\,\mathbf{\Omega}_p \times \mathbf{V}_p = \frac{\mathbf{F}_Q}{\rho_l \mathcal{V}_p} + (\Gamma - 1)g\hat{\mathbf{e}}_j, \qquad 9.$$

$$\left(\frac{1}{10}I^* + B_2\,\delta\right)\frac{d\mathbf{\Omega}_p}{dt} = \frac{\mathbf{T}_Q}{\rho_p \mathcal{V}_p d_p^2}, \qquad 10.$$

where $\mathbf{V}_p$ is the sphere velocity vector; $\mathbf{\Omega}_p$ is the sphere angular velocity vector; g is the acceleration due to gravity; and $I^* \equiv I_p/I_l$ is the moment of inertia ratio, with I_p the sphere moment of inertia and I_l the moment of inertia of the liquid volume displaced by the spherical particle. $\mathbf{F}_Q$ and $\mathbf{T}_Q$ represent the quasi-static fluid force and torque vectors, respectively, which result from the existence of vorticity in the flow. These terms can be straightforwardly obtained by integrating the local stress and moment over the sphere surface. Note that $\delta = \sqrt{(\nu\tau_v)/(\pi d_p^2)}$ is the dimensionless Stokes boundary layer, which develops in a time τ_v. The prefactors $B_1 = 18$ and $B_2 = 2$ are analytically obtained from unsteady viscous contributions (73, 84). Equations 9 and 10 help us appreciate the strong coupling that could exist between the translation and rotation of a buoyant spherical particle ($I^* \sim \Gamma < 1$). Assuming the time available for the Stokes layer to develop scales with the vortex shedding timescale, Mathai et al. (65) estimated that, up to moderate Ga, the role of I^* ought to be insignificant. By contrast, upon increasing Ga further, I^* becomes increasingly dominant in Equation 10.

3.3.3. Rotation-induced accelerations. To further analyze the role of rotation, it is advantageous to adopt a Lagrangian frame of reference that is oriented with respect to the sphere's instantaneous motion (**Figure 8d**). The mutually orthogonal Frenet–Serret coordinates are the tangent $\mathbf{T} = \dot{\mathbf{x}}_p/|\dot{\mathbf{x}}_p|$, normal $\mathbf{N} = \mathbf{B} \times \mathbf{T}$, and binormal $\mathbf{B} = (\dot{\mathbf{x}}_p \times \ddot{\mathbf{x}}_p)/\|\dot{\mathbf{x}}_p \times \dot{\mathbf{x}}_p\|$ vectors, which are directed along the particle velocity, curvature, and a direction perpendicular to the trajectory plane, respectively. For neutrally buoyant spheres in turbulence, Zimmermann et al. (79) were the first to show the existence of an alignment between translation and rotation. **Figure 8e** and the inset show PDFs of linear (a_N) and angular accelerations (α_N), respectively, of two buoyant spheres ($\Gamma \approx 0.89$) that differ solely in their rotational inertia ratios, $I^* = 1.0$ and 0.6. For the case of lower I^*, a strong coupling between translation and rotation ensues, which is strongly reflected in the particle's linear and angular acceleration PDFs (65). The same qualitative effects were reproduced for buoyant cylindrical particles with different I^* values (67). New experiments are being extended to the realm of buoyant ellipsoidal particles (oblate to prolate) in turbulence (J. Will, V. Mathai, D. Krug, S. Huisman, D. Lohse & C. Sun, unpublished manuscript). Interesting new regimes are being revealed (**Figure 9**) due to the coupling among particle buoyancy, particle shape, and turbulence.

3.4. Lift- and Shear-Induced Lateral Migration

It is well known that bubbles or buoyant particles experience a lift force when subjected to a mean shear in a flow. For spherical particles rising in a simple shear flow, the nature of these lift forces is by now well understood (86, 87). The case of bubbles, however, is quite different due to additional complexities arising from deformability, internal circulations, and surface contamination (50, 88–92). In most situations, the aim is to assess the lateral forces that induce bubble migration toward
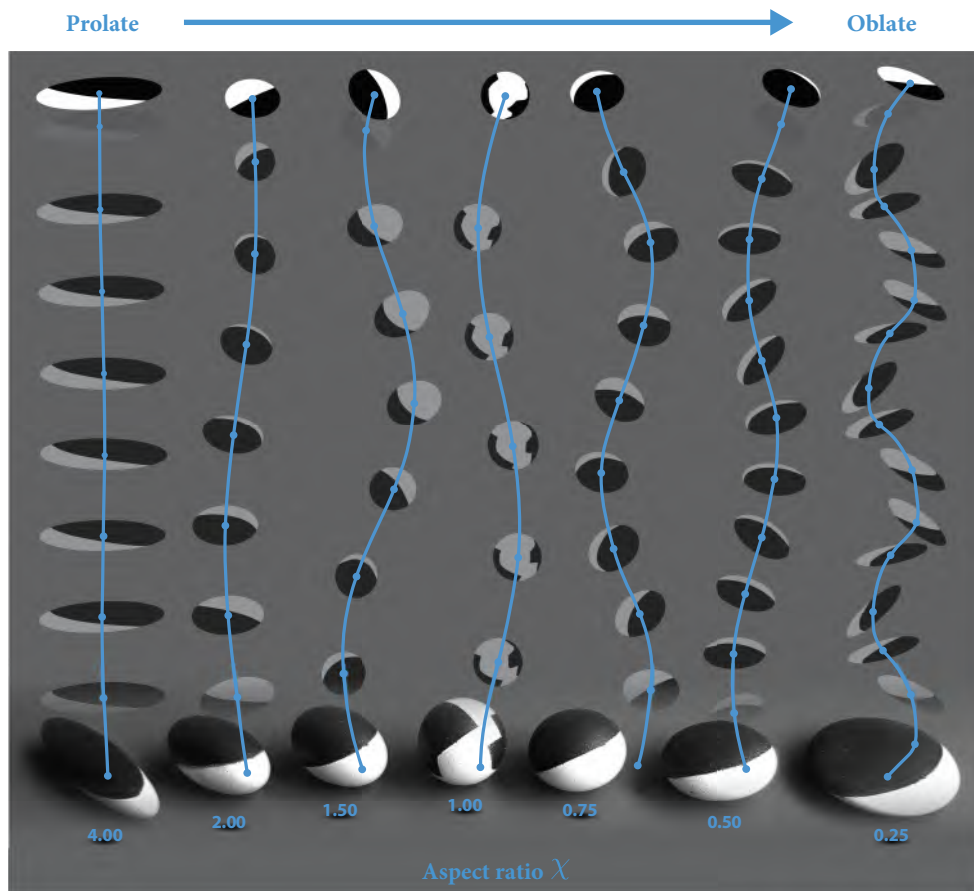
Figure 9

Trajectories of buoyant ellipsoids of different aspect ratios χ rising in quiescent liquid. The observed
trajectories are remarkably robust to background turbulent fluctuations. Here, $\Gamma = 0.8$ and $Ga = 300$,
calculated on the basis of the diameter $d_{pe} = (6\mathcal{V}_p/\pi)^{1/3}$. Aspect ratio χ is used to distinguish oblate ($\chi < 1$)
and prolate ($\chi > 1$) ellipsoids from a spherical particle ($\chi = 1$). The oblate ellipsoids represent an
approximation of the mean deformed shapes of millimetric air bubbles in water (77, 85). Figure adapted
from J. Will, V. Mathai, D. Krug, S. Huisman, D. Lohse & C. Sun (unpublished manuscript).

or away from the wall, which in turn can be expressed as a function of bubble properties (de-
formability, size), and flow properties (coflowing channel, counterflowing channel, or background
turbulence level).

Bubble-laden wall layers are a common observation and have been extensively explored exper-
imentally (93–96). In the presence of turbulence, the two most common flow configurations are
upward (97) and downward (98) turbulent channel flows. Whereas in single-phase flow the two are
identical, they differ greatly for two-phase situations, since the bubble buoyancy can now orient
differently with respect to the mean shear near the channel walls. Drew & Lahey (99) developed
the first model to unveil the mechanisms involved. Using an asymptotic analysis, they qualitatively
reproduced the general trends for the velocity profiles and void fraction distributions. In compari-
son, DNS provide an ideal setting in which the governing NS equations can be solved numerically
for both phases such that all the length and timescales are fully resolved. Lu et al. (100) used DNS
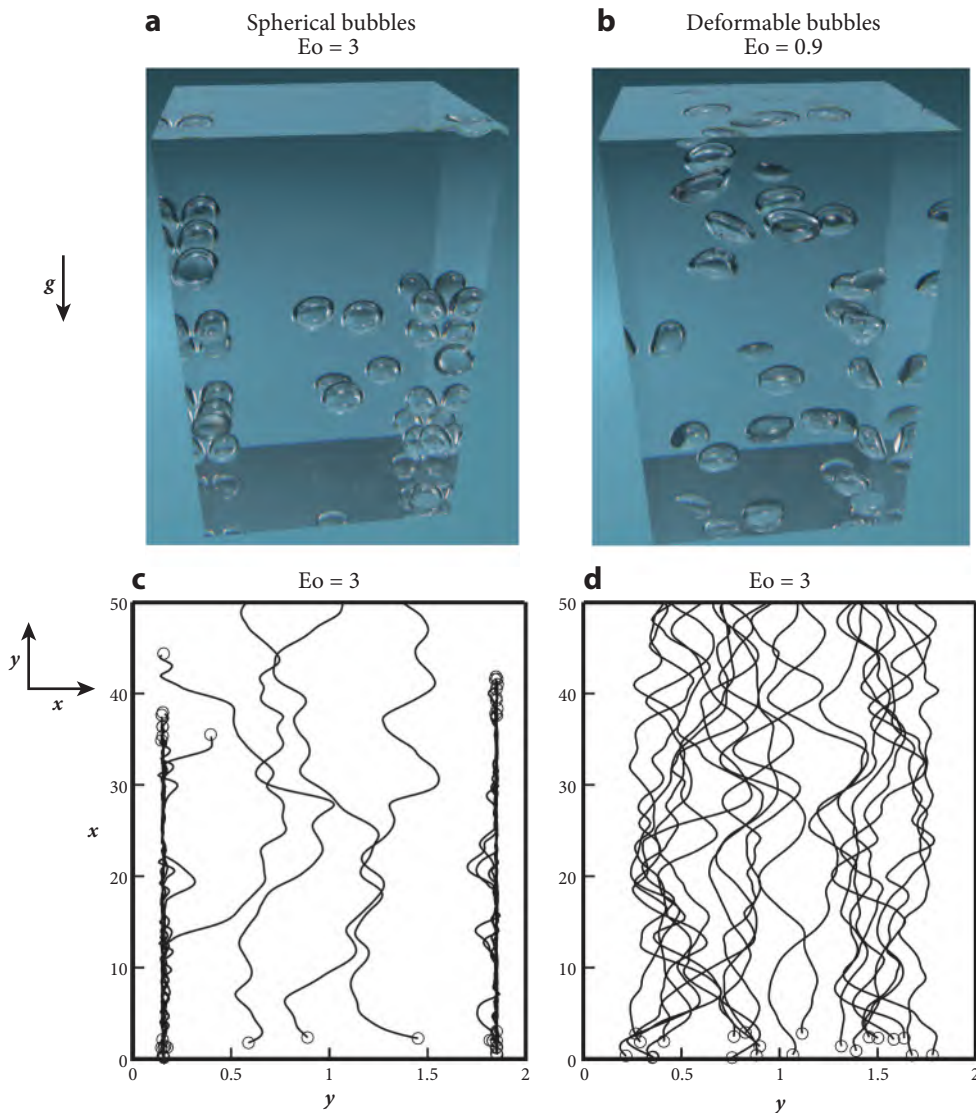
Figure 10

Direct numerical simulations of rising bubbles in vertical channel flows. Distribution of (*a*) spherical (Eo = 3) and (*b*) deformable (Eo = 0.9) bubbles, respectively, in an upward flow turbulent channel at a friction Reynolds number of $Re_\tau = 127$. The ratio of bubble diameter to channel half-width is $d_p/b = 0.3$, and the mean bubble Reynolds number is $Re_p \approx 136$. Spherical bubbles migrate toward the walls, but deformable bubbles distribute themselves nearly uniformly in the bulk of the flow, as demonstrated by the tracks of the (*c*) spherical and (*d*) deformable bubbles. Figure adapted from Reference 102.

with front tracking to examine bubbly flows in a vertical channel. The results showed that for nearly spherical bubbles, the lift-induced lateral migration resulted in two regions: a nearly uniform velocity bulk flow region, in which the weight of the liquid–bubble mixture balances the imposed pressure gradient, and a wall layer, which is free of bubbles for downflow and bubble-rich for upflow (101). The latter situation, with bubble clustering near the walls, is shown in **Figure 10***a*.

While this result can be explained in the same spirit as the shear-induced lift of rigid spherical particles, strikingly, when the bubble is deformable the effect is reversed (**Figure 10*b***), and deformable bubbles distribute themselves in the bulk of the channel. The negligible lift for the deformable bubble can be attributed to the pliant nature of its interface, which prevents the buildup of a nonuniform surface pressure distribution. Thus, it is bubble deformability (103), and not size, that causes the sign change of the lift force in turbulent upflow channels and pipes. We return to the flow modifications that the bubbles bring about in vertical channel flows in Section 4.2.2, below.

4. TURBULENCE MODULATION BY BUBBLES

Above, we have reviewed a variety of regimes for bubbles and buoyant particles in turbulent flows. However, it is the collective behavior of these particle that often contributes to sizable effects in most engineering applications of particle-laden turbulence. We now discuss the crucial role that some of the above-described mechanisms play in triggering the different kinds of flow modulations occurring in low– to moderate–volume fraction ($\alpha < 5\%$) suspensions of bubble-laden turbulence.

4.1. Bubbles Rising Within Homogeneous Turbulence

Two forms of turbulent flows with statistical homogeneity, namely HIT and homogeneous shear turbulence, are considered in Sections 4.1.1 and 4.1.2, respectively.

4.1.1. Homogeneous isotropic turbulence.
HIT represents one of the most elementary forms of turbulence imaginable (104). Notwithstanding how unrealistic this flow might seem from a practical viewpoint, studies of HIT have led to great breakthroughs in our understanding of real-world turbulent flows (23). The assumptions of statistical homogeneity and isotropy (among others) have been central to many successful theories of turbulent flows. Note that all single-phase flows, at high enough Reynolds numbers, will behave as HIT in the universal range and far from boundaries. For single-phase turbulence, the $-5/3$ scaling of the energy spectrum (in the inertial range) is well known (23); here, the energy flux flowing down to smaller length scales is nearly constant up to the dissipative scales. In contrast, for a swarm of high-Re_p bubbles rising within an otherwise quiescent liquid, bubble-induced turbulence (BIT) leads to a -3 scaling for the energy spectrum. This result, originally observed in the milestone study by Lance & Bataille (105), has by now become well established through detailed experiments, DNS, and even large-eddy simulations (106–108b). A further simplified approach was undertaken by Mazzitelli & Lohse (109), who used the PP equation of motion with an imposed back reaction on the flow. This cumulative back-reaction force, $\mathbf{f}_R = \Sigma[(D\mathbf{u}/Dt) - g]\mathcal{V}_p \, \delta(\mathbf{x}_f - \mathbf{x}_p)$, acting at the point $\mathbf{x}_f$ in the flow, did not generate the kind of liquid agitation commonly observed in BIT. Although the two-way coupling proved nonideal for BIT, it demonstrated that the key component for the scaling (missing in the PP approach) was a model for the unsteady bubble wakes. For a detailed review of the liquid agitation induced by bubble swarms (BIT), see Reference 68.

Single-phase turbulence and bubbly swarms have been studied separately, but the situation where bubbles are injected into an already turbulent background flow, despite its relevance in industrial applications, has only recently begun to be understood. What determines the nature of the liquid fluctuations and energy spectrum of such bubbly turbulent flows? To allow comparisons across different levels of turbulence and bubble volume fractions, Lance & Bataille (105) [and later Rensen et al. (110)] introduced the so-called bubblance parameter, *b*, which compares the intensity of BIT with the intensity of incident turbulence. This ratio of kinetic energies can
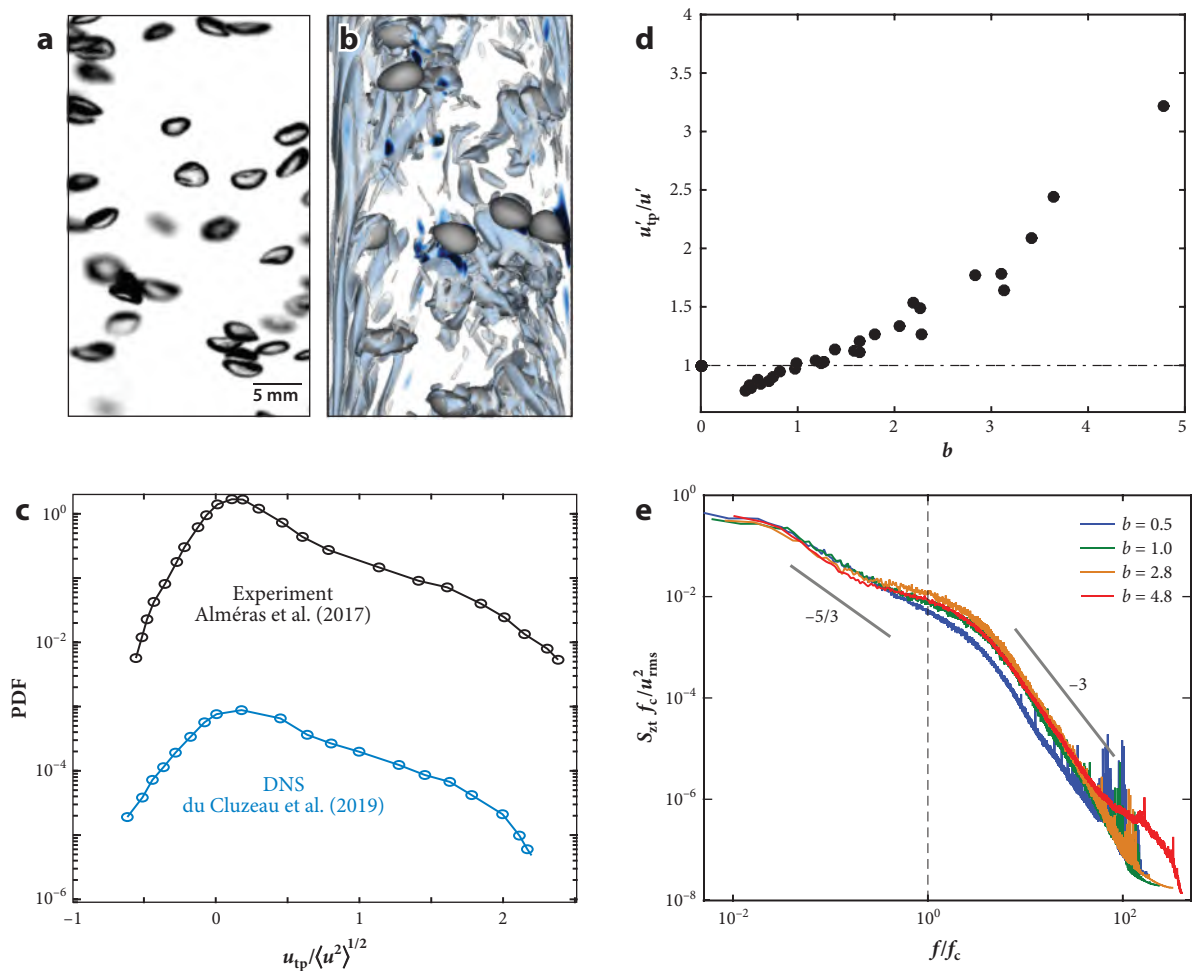
Figure 11

Flow modification in turbulent bubbly upflows. (*a*) Experimental images of 2–4-mm-diameter deformable air bubbles in a vertical flow at $Re_\lambda = 262$. (*b*) Volume rendering of deformable bubbles in a turbulent flow, obtained from direct numerical simulations (DNS) with the front tracking method. The flow structures are colored by isovalues of the so-called λ_2 criterion (114). (*c*) Probability density functions (PDFs; vertically shifted for better visibility) of the axial velocity in the bulk of the flow from the experimental (*black*) and DNS (*blue*) cases shown in panels *a* and *b*, respectively. The PDF shapes are qualitatively similar in the experiments and DNS. (*d*) Normalized vertical velocity fluctuations of the liquid phase for different values of the bubblance parameter, *b*. (*e*) Normalized spectra of the bubble-induced liquid fluctuations. Distinct ranges of scalings can be observed: $-5/3$ for $f/f_c < 1$ and -3 for $f/f_c > 1$. f_c is a characteristic cutoff frequency, which can be calculated using the bubble and flow properties. Panels *a*, *d*, and *e* adapted from Reference 112. Panel *b* adapted from Reference 113.

be written as $b = \alpha \bar{V}_r^2 / u'^2$, where $\bar{V}_r$ is the mean rise velocity of the bubbles.[2] Recently, Alméras et al. (112) conducted extensive experiments in such turbulent bubbly flows for a wide range of *b*. **Figure 11*a*** depicts 2–4-mm-diameter bubbles rising in the bulk region of upward channel flow. The liquid velocity fluctuations in bubble-laden turbulence was measured using phase-sensitive

---

[2]Note that a prefactor of $1/2$, based on the C_M of a spherical bubble (111), was used in the definition of *b* in Reference 110.

hot-film anemometry (112) and shown to be positively skewed as is also the case for BIT. Similarly skewed velocity PDFs have been observed in DNS of bubbles in turbulent upflows (113) by use of the front tracking method (**Figure 11*b,c***). In the experiments, turbulence attenuation was observed at low values of b (<0.25), while the liquid velocity fluctuations were augmented at high b (**Figure 11*d***). We emphasize that the liquid agitation produced by high–Reynolds number bubbles is anisotropic (68), the effects of which are also noticeable in turbulent flows. For details about the anisotropy of liquid velocity fluctuations in bubble-laden turbulence, see Reference 115.

With knowledge of the magnitude and distributions of liquid agitation, the natural next question is: How is the energy spectrum modified by the presence of bubbles in an incident turbulent flow? **Figure 11*e*** shows the spectrum of liquid velocity fluctuations for b in the range $[0, 1.3]$. With the addition of bubbles, the higher frequencies of the inertial subrange of single-phase turbulence are substituted by a -3 scaling of BIT. However, the $-5/3$ scaling appears to be preserved for the lower frequencies for all values of b tested. The characteristic cutoff frequency, f_c, imposed by the bubble swarm may then be calculated as $\bar{V}_r/\lambda_c$, where $\lambda_c = d_p/C_{d0}$, with C_{d0} the drag coefficient of an isolated bubble in still fluid (116). The above results only partially resolve the complexity of the problem. The spectrum modification by 2–4-mm-diameter bubbles (reported above) is at variance with some of the observations in Reference 68. The reason involves the differences in the operating conditions, specifically the size and Reynolds number of the bubbles. A change in bubble diameter leads to a different cutoff length scale, λ_c. This leaves room for much variability in the frequency range of BIT. These issues can be resolved through careful studies in which bubble size and bubble Reynolds number are controlled independently. Such studies will, however, be challenging.

4.1.2. Homogeneous shear turbulence.

Homogeneous shear turbulence can be considered one of the simplest turbulent flows, in that the flow relaxes the condition of statistical isotropy but maintains homogeneity over all spatial scales (117, 118). Explorations of bubble-laden homogeneous shear turbulence have been performed mainly using direct numerical simulations (119). As a general rule, bubbles enhance the dissipation rate of turbulent kinetic energy (120); however, the production rate of turbulent kinetic energy can be either enhanced or diminished, depending on the flow parameters (121). While the turbulent kinetic energy production rate increases with turbulent Reynolds number, it decreases with shear Reynolds number. In addition, bubble deformability enhances the turbulent kinetic energy production rate. Although simplified models have been proposed to explain these observations, the absence of direct experimental evidence has led to much debate regarding the validity of these mechanisms in causing turbulence modulation.

4.2. Bubble-Laden Channel Flows

Channel flows are an extremely important class of turbulent flows, owing to their widespread presence in industrial and engineering settings. Based on the orientation of the channel with respect to gravity, they can be broadly classified into horizontal channels (Section 4.2.1) and vertical channels (Section 4.2.2). We review some of the flow modifications that result from the addition of bubbles to these canonical flow configurations.

4.2.1. Horizontal channels and boundary layers.

Several experimental explorations over the past few decades (122–125) have demonstrated that the injection of bubbles, small or large, in turbulent boundary layers and horizontal channel flows modulates flow. Recent numerical studies have employed either Eulerian–Lagrangian models (126, 127) or DNS (128) to show that bubbles
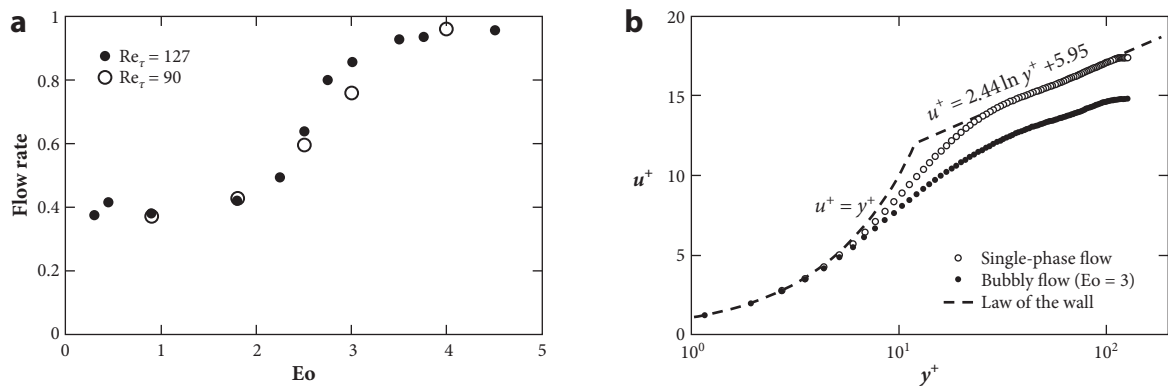
Figure 12

Flow modification in turbulent bubbly upward channel flows for a 3% volume fraction of bubbles with a size ratio $d_{\mathrm{p}}/h = 0.3$, where h is the channel half-width. (*a*) Flow rate as a function of bubble deformablity, quantified here using the Eötvös number (Eo, also known as the Bond number, Bo), for two different values of the friction Reynolds number (Re$_\tau$). The Re$_\tau$ effect is negligible; the phenomenon is governed primarily by the bubble deformability. The bubble Reynolds number (Re$_\mathrm{p}$) lies in the range [120, 200]. (*b*) Velocity profile near the wall for the Eo = 3 (Re$_\tau$ = 127) case in panel *a*, in comparison to the single-phase case. Figures adapted from Reference 102.

can modify near-wall vortical structures, causing friction drag reduction even with relatively low volume fractions. For reviews on drag reduction by bubbles in turbulent boundary layers, see References 4, 129, and 130.

4.2.2. Vertical channels. Turbulence modulation in bubbly vertical channel flows has historically been the subject of numerous investigations, both experimental (131) and analytical (132). As discussed in Section 3.4, above, with high-resolution DNS becoming increasingly feasible, simulations employing front tracking (133) have led to significant breakthroughs in our understanding of these problems (113, 134–137). Here, we describe the main effects of bubbles on the underlying flow field.

For a bubble-laden channel flow, the relevant dimensionless parameters are Re$_\mathrm{h}$, Ga, and Eo. The bubble Reynolds number, Re$_\mathrm{p}$, which is one of the output parameters, can be expressed as a function of Ga, Eo, and to a lesser extent the volume fraction α. For upward channel flows, the most prominent effect is a reduction in the net flow rate. This reduction is most extreme for spherical bubbles, since they occupy the near-wall regions. Highly deformable bubbles, owing to their nearly zero (or slightly negative) lift force, remain in the bulk of the flow, thus having negligible effect on the volumetric flow rate (**Figure 12a**). The physical mechanism behind the flow rate reduction is a sudden rise in the near-wall viscous dissipation when the spherical bubbles enter the viscous sublayer. As determined by their relative distributions, the near-wall liquid velocity fluctuations are enhanced for spherical bubbles, but the same occurs in the bulk for deformable bubbles. In addition, turbulent velocity fluctuations in the bubble-rich regions are enhanced, a result arising directly from knowledge of BIT (68). The velocity profile near the wall is retarded in the presence of bubbles (**Figure 12b**), which is consistent with the observed flow rate reductions. In the less commonly explored downflow configuration with bubbles (100), a flow rate reduction is accompanied by a suppression of turbulence in the near-wall bubble-free layer as well as by turbulence augmentation in the bubble-rich bulk flow (see also Section 3.4). Thus, while in many engineering applications it might seem beneficial to reduce bubble size and maximize the interfacial area, such efforts should not be made at the expense of flow rate reduction due to viscous losses of the bubbles accumulating near the wall.

Lastly, we note that the above discussion pertains to clean bubbles. In reality, the void fraction profiles in turbulent bubbly upflow experiments (131) may not be as sharply peaked as seen in simulations (DNS). When the gas–liquid interfaces are contaminated (with dirt or surfactants), one can expect a slight reduction in lift force and lateral migration tendency (138–140). Thus, even at low volume fractions of the dispersed phase, bubble dynamics can show fundamental differences from particles because of the presence of an internal circulation. In contrast, dense bubbly flows ($\alpha \geq 5\%$) must be treated as a markedly different subject; for a review of experiments on bubbles in vertical pipe/channel flows, see Reference 141. For a review of flow regimes, operating parameters, and design parameters of industrial bubble columns, see Reference 142.

4.3. Bubbly Taylor–Couette Turbulence

Taylor–Couette (TC) flow, the flow between two coaxial co- or counterrotating cylinders, is one of the paradigmatic systems of fluid physics (143). Unlike the turbulent flows discussed above, TC flow is a closed system with exactly derivable balances between driving and dissipation. Owing to these particular benefits, turbulent TC flow experiments have been widely used as a model system to study bubble-induced flow modulations, bubble–vortex interactions, and bubbly drag reduction (144–150). A remarkable effect of introducing bubbles in turbulent TC flow is that one can achieve significant turbulence modulation with only a small percentage [$\alpha \sim \mathcal{O}(1\%)$] of bubbles. This usually manifests in major drag reduction, with various mechanisms contributing to it (see also 14, section 9).

4.3.1. Drag reduction in the buoyancy-dominant regime. We now turn to studies on drag reduction by microbubbles in turbulent TC flow. To this end, Sugiyama et al. (151) and Spandan et al. (152) conducted DNS employing an Euler–Lagrangian (PP) two-way coupled approach in a regime where the inner cylinder Reynolds number, $\mathrm{Re}_{\mathrm{ic}} \equiv \omega_{\mathrm{ic}} r_{\mathrm{ic}} (r_{\mathrm{oc}} - r_{\mathrm{ic}})/\nu$, was in the range [600, 8,000]. Here, ω_{ic}, r_{ic}, and r_{oc} are the inner cylinder angular velocity, inner cylinder radius, and outer cylinder radius, respectively. The drag reduction was defined as

$$\mathrm{DR}(\%) = \frac{\langle C_{\mathrm{f}} \rangle_{\mathrm{s}} - \langle C_{\mathrm{f}} \rangle_{\mathrm{tp}}}{\langle C_{\mathrm{f}} \rangle_{s}} \times 100, \qquad 11.$$

where $C_{\mathrm{f}} = [(1 - r_{\mathrm{ic}}/r_{\mathrm{oc}})^2 / \pi] G / \mathrm{Re}_{\mathrm{ic}}^2$ is the friction factor and $G = \tau/(2\pi \ell_{\mathrm{c}} \rho_1 \nu^2)$ is the dimensionless torque, with τ the torque that is necessary to keep the inner cylinder of length ℓ_{c} rotating at constant angular velocity (153). The subscripts s and tp denote single phase and two phase, respectively. Simulations by Sugiyama et al. (151) and Spandan et al. (152) have shown that the buoyant motions of microbubbles can disrupt the coherent vortices (i.e., Taylor rolls), resulting in a reduction of drag (up to 20%) on the inner cylinder surface (**Figure 13a**). Spandan et al. (152) varied the Froude number, $\mathrm{Fr}_{\mathrm{ic}} = \omega_{\mathrm{ic}} \sqrt{r_{\mathrm{ic}}/g}$, which represents the ratio of centripetal force strength over buoyancy force, in the range [0.16, 2.56]. By keeping the values of $\mathrm{Re}_{\mathrm{ic}}$, α, and d_{p} fixed, the authors found that drag reduction was at low values of $\mathrm{Fr}_{\mathrm{ic}}$ ($\mathrm{Fr}_{\mathrm{ic}} \lesssim 1$) and negligible at high values ($\mathrm{Fr}_{\mathrm{ic}} \gtrsim 1$). In this regime, drag reduction decreases with increasing Reynolds number. For a more generic quantification of drag reduction in this low–Reynolds number regime, one might incorporate the bubble St and α as well, in which case the drag reduction can likely be expressed as a function of St/Fr and α (assuming the bubbles are noninertial). The aim is to obtain an overarching dimensionless parameter that can explain the degree of drag reduction in the so-called wavy vortex regime (154–156) of TC turbulence.

4.3.2. Drag reduction in the highly turbulent regime. In the high-$\mathrm{Re}_{\mathrm{ic}}$ regime, the stable coherent structure of the vortices in TC turbulence no longer persists. Consequently, the effect of the
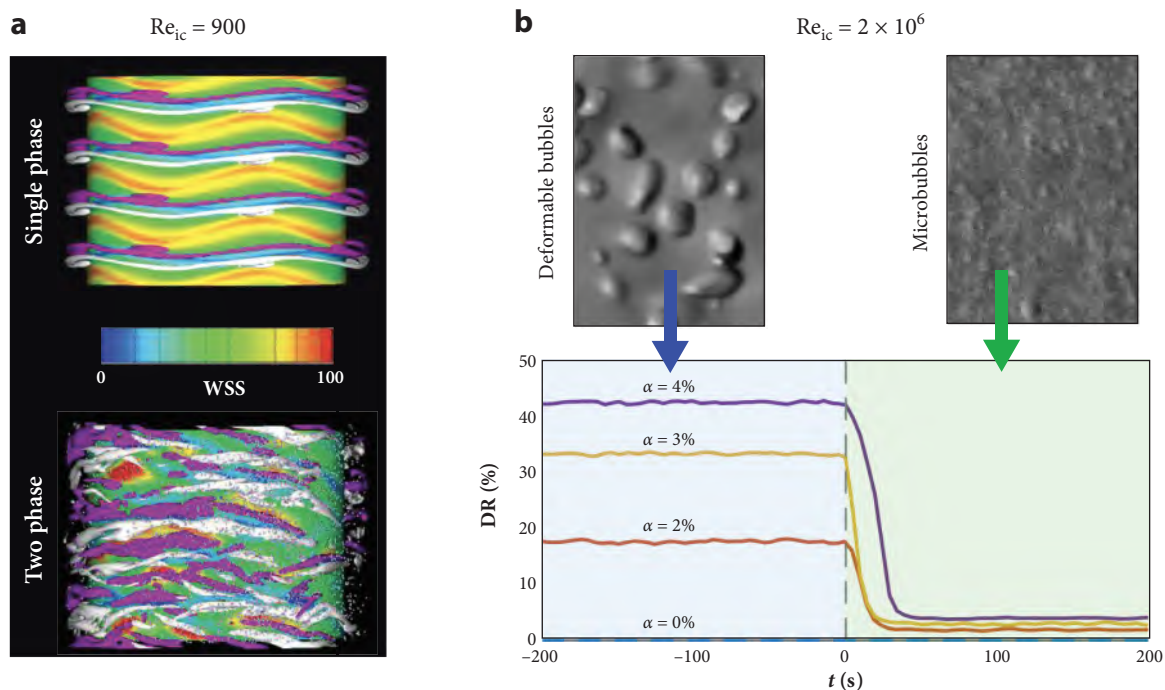
Figure 13

Bubbly drag reduction (DR) in turbulent Taylor–Couette (TC) flow. (*a*) Direct numerical simulations of TC turbulence at an inner cylinder Reynolds number (Re_{ic}) of 900 for (*top*) single-phase flow and (*bottom*) two-phase flow laden with pointlike bubbles. Wall shear stress (WSS) (*color bar*) is reduced in the two-phase flow with small bubbles, leading to ~20% DR. (*b*) DR as a function of time at high Re_{ic} values ($Re_{ic} = 2 \times 10^6$). Nearly all DR is lost after injection of a surfactant (Triton X-100), which reduces the two-phase flow from a suspension of large deformable bubbles (*upper left inset*) to microbubbles (*upper right inset*). Panel *a* adapted from Reference 151. Panel *b* adapted from Reference 144.

bubbles on friction drag diminishes, as mentioned above. However, bubbles can still be used to reduce drag in the highly turbulent TC regime. In this high–Reynolds number regime, however, the deformability of the bubble (i.e., We > 1) is crucial for drag reduction (147, 148). In this regime, drag reduction increases with increasing Re_{ic}. Verschoof et al. (144) provide a direct experimental demonstration of the effects of bubble deformability on turbulent TC drag reduction. These authors dynamically changed the drag by adding a minute amount of surfactant (Triton X-100) to a highly turbulent TC flow (up to $Re_{ic} = 2 \times 10^6$) laden with deformable bubbles (**Figure 13*b***). In the original state with only a 4% volume fraction of deformable bubbles, the drag reduction was more than 40%. The addition of surfactant initiated a remarkable turn of events (breakup, coalescence prevention, etc.) that caused the large deformable bubbles to be fully substituted by tiny microbubbles. This reduced the drag reduction to only 4%, which corresponds to the trivial effect of the bubbles on the density and viscosity of the liquid.

Spandan et al. (157) recently used DNS to investigate the physical mechanisms of drag reduction in the turbulent regime (up to $Re_{ic} = 2 \times 10^4$). They connected the increase in drag reduction to a decrease in the dissipation in the wake of highly deformed bubbles near the inner cylinder. This interpretation can be linked to the more familiar field of polymer drag reduction (158–160) and suggests possible similarities in drag reduction mechanisms where the elastic properties of the dispersed phase are exploited.

Yet another important issue that arises in studies of bubbly drag reduction in TC flow is the effect of centripetal force on the bubble distribution in the flow. If the TC flow is in a fully laminar state (and $\mathrm{Fr}_{ic} \gg 1$), all the bubbles should be pushed against the inner wall due to the radial pressure gradient induced by the centrifugally driven flow. However, when the system is a highly turbulent state, the bubbles experience liquid velocity fluctuations and pressure fluctuations, which are enough to diffuse them toward the bulk region of the flow (148). The resulting bubble distribution in the gap between the cylinders will depend on the competing effects of the turbulent pressure fluctuations: induced acceleration, a_{pf}, and centripetal acceleration, $a_c(r)$. The competition between these two terms can be expressed as a so-called[3] centripetal Froude number:

$$\mathrm{Fr}_c(r) = \frac{a_{\mathrm{pf}}}{a_c(r)} = \frac{u'^2/d_p}{U_\theta^{2/r}}, \qquad 12.$$

where U_θ is the mean azimuthal liquid velocity and r is the radial position in the TC setup under consideration. van Gils et al. (148) estimated that $\mathrm{Fr}_c \approx 1.6$ at $\mathrm{Re}_{ic} \sim 5 \times 10^5$ and that $\mathrm{Fr}_c \approx 3.4$ at $\mathrm{Re}_{ic} = 1 \times 10^6$. The lower Re_{ic} implies a lower Fr_c, so the effective centripetal force on the bubbles is higher and the bubble accumulation, in turn, is stronger near the inner cylinder wall at the expense of a lower concentration in the bulk. This reasoning is also consistent with these authors' direct experimental observations.

Thus, drag reduction in bubbly TC turbulence is a function of several parameters. While at moderate Re_{ic} the buoyancy-induced drift of the microbubbles is sufficient, in the highly turbulent regime buoyancy, deformability, and centripetal effects are all crucial components of drag reduction. In light of the close analogy between TC flows and pipe flows (161), the results obtained for turbulent TC flows are valuable for research on drag reduction. However, it remains to be determined whether and how the principles of turbulent two-phase TC flow can be extended to pipelines and naval applications.

4.4. Bubbles in Turbulent Convection

In heat transfer systems, the motion of bubbles can efficiently induce mixing of warm and cold parcels of liquid. For many industrial applications, injecting bubbles into the flow can lead to a 100-fold enhancement in the heat transfer coefficient in comparison to its single-phase counterpart (162). Therefore, the effect of bubbles and light particles on heat transfer has been the subject of several experimental and numerical investigations. One approach to enhancing heat transport is to create vapor bubbles (16) or biphasic (163) and thermally expandable (164) particles. Some of these approaches have resulted in impressive heat transport enhancements in comparison to the single-phase case (163, 165, 166). However, in this review we restrict our attention to gas-phase bubbles.

Early studies in forced convection systems with bubble injection (167–169) showed that the bubbles modify the temperature profile of the system and that the gas volume fraction close to the heated wall is important for heat transfer enhancement; in other words, higher void fractions close to the heated wall lead to enhanced heat transfer. Using DNS with front tracking, Dabiri & Tryggvason (170) recently studied the effect of bubbles on the heat transfer rate in a flow between two parallel walls under a constant heat flux condition. They found that the bubbles stir up the viscous layer and reduce the size of the conduction region near the wall, resulting in improved

---

[3]Note that this Froude number should not be confused with the more widespread definition of Froude number, where the gravitational force appears in the denominator. Here, the body force in the denominator is centrifugal.

heat transfer efficiency; in other words, a 3% volume fraction of bubbles can increase the Nusselt number by 60%.

Studies of the effects of bubble injection on heat transfer in natural convection systems have been conducted mostly with injections of microbubbles (171, 172) and submillimetric bubbles (173) close to the heated wall. Kitagawa & Murai (173) investigated the effects of microbubble injection on natural convection heat transfer from a vertical heated plate in water. They found that microbubble injection significantly increases the heat transfer coefficient in both the laminar and transition regimes. The enhancement ratio of the heat transfer coefficient due to bubble injection is 1.6–2.0 in the laminar regime and 1.5–2.0 in the transition regime. The physical reason for heat transfer enhancement in the laminar regime is effective mixing, whereas the physical reason for the heat transfer enhancement in the transition region is that microbubble injection accelerates the transition to turbulence (173). Using DNS, Deen & Kuipers (174) studied wall-to-liquid heat transfer in dispersed gas–liquid two-phase flow and found that a few high–Reynolds number bubbles rising in quiescent liquid can considerably increase local heat transfer between the liquid and a hot wall.

Recently, Gvozdić et al. (5) studied the effect of deformable bubbles (with diameters of 2–3 mm) on heat transfer in a vertical natural convection setup, which was heated from one side and cooled from the other side (**Figure 14a**). The air bubbles were injected into the system using 180 capillaries (inner diameter, 0.21 mm) uniformly distributed over the bottom of the natural convection system. The gas volume fraction, α, varied from 0.5% to 5%, and the Rayleigh number ranged from 4.0×10^9 to 3.6×10^{10}. Here, the Rayleigh number is defined as $\mathrm{Ra}_H = [g\gamma(\overline{T_h} - \overline{T_c})H^3]/\nu\kappa_c$, and the Nusselt number is defined as $\overline{\mathrm{Nu}} = (Q_c/A)/[K(\overline{T_h} - \overline{T_c})/L]$, where γ is the thermal
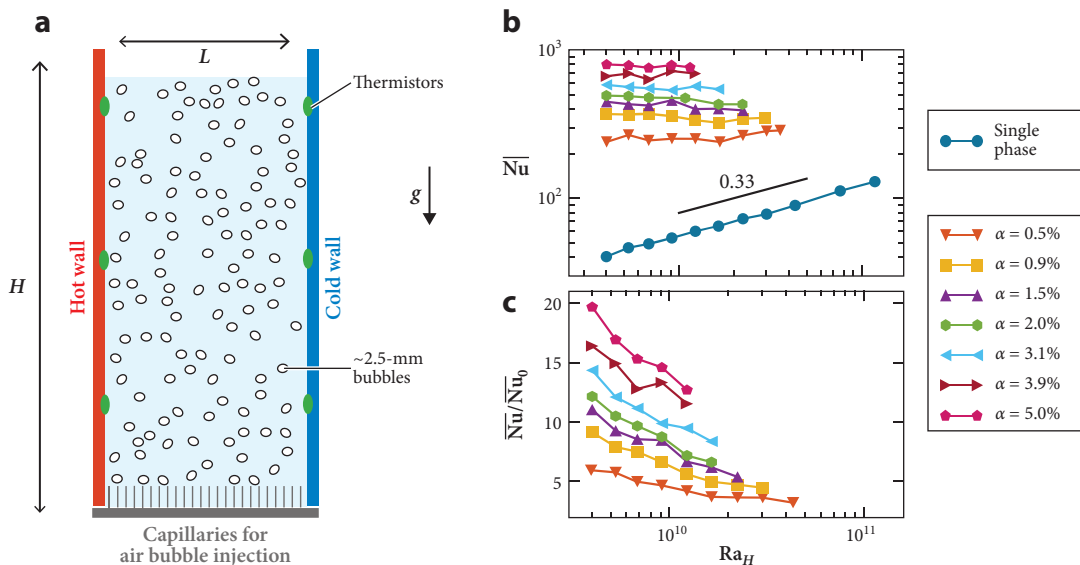
Figure 14

(*a*) A turbulent vertical convection setup (experiment) with bubble injection. The rectangular bubbly column is heated from one side of the wall and cooled from the other side; the height (*H*) is 600 mm, and the length between the heated and cooled side walls (*L*) is 230 mm. Bubbles with diameters of ~2.5 mm were injected into the system through 180 capillaries (inner diameter, 0.2 mm) placed at the bottom of the apparatus. (*b*) Nusselt number ($\overline{\mathrm{Nu}}$) in bubble-laden vertical convection versus Rayleigh number (Ra_H) for various gas volume fractions α. The blue circles, shown for comparison, correspond to the single-phase turbulent vertical convection case ($\alpha = 0\%$). The size of the symbols corresponds to the typical error bar in the data. (*c*) Heat transfer enhancement due to bubble injection $\overline{\mathrm{Nu}}/\overline{\mathrm{Nu}_0}$ versus Ra_H. Here, $\overline{\mathrm{Nu}_0}$ is the Nusselt number of the single-phase case. Figure adapted from Reference 5.

expansion coefficient; $\overline{T}_{h}$ and $\overline{T}_{c}$ are the mean temperatures of the hot and cold walls, respectively; L is the length of the setup; A is the surface of the sidewall; κ_{c} is the thermal diffusivity; K is the thermal conductivity of water; and Q_{c} is the measured power supplied to the heaters. For the entire range of α and Ra_{H}, adding bubbles dramatically increased the heat transport efficiency, as the Nusselt number is approximately an order of magnitude higher than in the single-phase flow case (**Figure 14b**). To more clearly quantify the heat transport enhancement due to bubble injection, **Figure 14c** shows the ratio of the Nusselt number for two-phase bubbly flow ($\overline{Nu}$) to that of the single-phase case ($\overline{Nu}_{0}$) as a function of Ra_{H} at different values of α. The figure shows that heat transfer was enhanced up to 20-fold as a result of the bubble injection and that the heat transfer enhancement increased with increasing α and decreasing Ra_{H}. Note that the decreasing trend of $\overline{Nu}/\overline{Nu}_{0}$ with Ra_{H} occurred because $\overline{Nu}_{0}$ increased with Ra_{H}, whereas $\overline{Nu}$ did not change with Ra_{H}. $\overline{Nu}$ was nearly independent of Ra_{H} and depended solely on α with the scaling of $\overline{Nu} \propto \alpha^{0.45}$, which suggests a diffusive transport mechanism, as has been found in the case of mixing a passive tracer into a homogeneous bubbly flow for a low gas volume fraction (6, 115). Thus, bubble-induced mixing dominates the efficiency of heat transfer in moderate-Ra_{H} bubbly natural convection systems.

SUMMARY POINTS

1. The past decade has witnessed tremendous progress in our understanding of bubbly and buoyant particle–laden turbulent flows. The addition of buoyant particles to turbulent flows can modify key aspects of single-phase turbulence, such as spectra or drag, offering the opportunity to use bubbles or light particles to tailor turbulent flows to our benefit.

2. As in many areas of modern fluid dynamics, fully resolved DNS can explain many intricate phenomena of two-phase turbulence. At the same time, a reduced treatment employing the Euler–Lagrangian approach proves sufficient in a remarkable number of situations. The basic PP formulation has been extended to include rotation through the Kelvin–Kirchhoff equations, which have significant predictive capabilities for buoyant particle and bubble dynamics in flows.

3. Deformable bubble dynamics in turbulence are governed by three fairly independent mechanisms: The average bubble shape is controlled mainly by the relative motion between the bubble and the surrounding fluid; the bubble's velocity and orientation are a result of its own wake instability; and the effect of turbulence is reflected by random deformations of the bubble interface, which under extreme situations can cause bubble breakup or rise velocity changes.

4. Buoyancy brings about a multitude of modifications to particle dynamics in turbulence. For small bubbles and particles, the crossing-trajectories effect leads to augmented particle accelerations, while in finite-sized and finite-Re_{p} cases, wake-induced accelerations add to the turbulent forcing. When the particle Reynolds number is increased, the buoyant particle's rotation further aids in the development of vigorous accelerated motions.

5. Addition of bubbles to turbulent flow is not synonymous with drag reduction. While bubbly drag reduction is possible in horizontal channel flows, boundary layers, and TC flows, in vertical channel flows (both upflows and downflows) the effective drag is enhanced. The reason is that in vertical channels the bubbles increase the energy dissipation rate, while in TC turbulence and other flows they suppress the dissipation.

6. Air bubbles added to (open) turbulent convection systems dramatically enhance heat transfer because of their induced liquid agitation and mixing.

FUTURE DIRECTIONS

1. Rigid buoyant anisotropic particles, including ellipsoidal, chiral, and vaned particles, can add significant amounts of energy to turbulent flows. Their coupled translational–rotational dynamics is crucial to liquid agitation.

2. Varying the rotational inertia and/or the center-of-mass location of buoyant particles presents exciting opportunities for turbulence modulation.

3. Whether or not the collective wake instabilities of rising bubbles and buoyant particles persist in intensely turbulent environments is an open question.

4. The issue of energy spectra in bubble-laden turbulence is only partially resolved. The effect of bubble size (in comparison to the Kolmogorov scale) is not clear. Similarly, spectrum modification by the wake of low– to moderate–Reynolds number bubbles remains to be elucidated. Furthermore, the behavior of bubbly turbulent flows in the limit of very high-intensity turbulence needs to be studied.

5. Tumbling buoyant particles can be engineered for turbulent downflow channels to affect near-wall turbulence and heat transfer. Bubbles cannot be used for this purpose.

6. The response of bubbles to homogeneous shear turbulence remains to be experimentally explored. The relative alignment between buoyancy and shear, in combination with deformability, is expected to induce symmetry breaking, and rich variability in bubble dynamics can be expected. These will require the design of dedicated experimental setups.

DISCLOSURE STATEMENT

The authors are not aware of any affiliations, memberships, funding, or financial holdings that might be perceived as affecting the objectivity of this review.

ACKNOWLEDGMENTS

LITERATURE CITED

1. Sengupta A, Carrara F, Stocker R. 2017. *Nature* 543:555–58
2. Calzavarini E, Huang YX, Schmitt FG, Wang LP. 2018. *Phys. Rev. Fluids* 3:054604
3. Thorpe SA, Hall AJ. 1987. *Nature* 328:48–51
4. Ceccio SL. 2010. *Annu. Rev. Fluid Mech.* 42:183–203
5. Gvozdić B, Alméras E, Mathai V, Zhu X, van Gils DP, et al. 2018. *J. Fluid Mech.* 845:226–44
6. Alméras E, Risso F, Roig V, Cazin S, Plais C, Augier F. 2015. *J. Fluid Mech.* 776:458–54

7. Toschi F, Bodenschatz E. 2009. *Annu. Rev. Fluid Mech.* 41:375–404
8. Voth GA, Soldati A. 2017. *Annu. Rev. Fluid Mech.* 49:249–76
9. Crowe C, Troutt T, Chung J. 1996. *Annu. Rev. Fluid Mech.* 28:11–43
10. Maxey M. 2017. *Annu. Rev. Fluid Mech.* 49:171–93
11. Elghobashi S. 2019. *Annu. Rev. Fluid Mech.* 51:217–44
12. Prosperetti A. 2015. *J. Fluid Mech.* 768:1–4
13. Elghobashi S. 1994. *Appl. Sci. Res.* 52:309–29
14. Lohse D. 2018. *Phys. Rev. Fluids* 3:110504
15. Balachandar S, Eaton JK. 2010. *Annu. Rev. Fluid Mech.* 42:111–33
16. Prosperetti A. 2017. *Annu. Rev. Fluid Mech.* 49:221–48
17. Veldhuis C, Biesheuvel A, van Wijngaarden L, Lohse D. 2004. *Nonlinearity* 18:C1
18. Ern P, Risso F, Fabre D, Magnaudet J. 2012. *Annu. Rev. Fluid Mech.* 44:97–121
19. Jha NK, Govardhan R. 2015. *J. Fluid Mech.* 773:460–97
20. Mazzitelli IM, Lohse D, Toschi F. 2003. *Phys. Fluids* 15:L5–8
21. Mazzitelli IM, Lohse D, Toschi F. 2003. *J. Fluid Mech.* 488:283–313
22. Maxey MR, Riley JJ. 1983. *Phys. Fluids* 26:883–89
23. Pope SB. 2000. *Turbulent Flow*. Cambridge, UK: Cambridge Univ. Press
24. Auton T, Hunt J, Prud'Homme M. 1988. *J. Fluid Mech.* 197:241–57
25. Rensen J, Bosman D, Magnaudet J, Ohl CD, Prosperetti A, et al. 2001. *Phys. Rev. Lett.* 86:4819–22
26. Calzavarini E, Volk R, Leveque E, Pinton JF, Toschi F. 2012. *Physica D* 241:237–44
27. Calzavarini E, Volk R, Bourgoin M, Leveque E, Pinton JF, Toschi F. 2009. *J. Fluid Mech.* 630:179–89
28. Homann H, Bec J. 2010. *J. Fluid Mech.* 651:81–91
29. Leal L. 1980. *Annu. Rev. Fluid Mech.* 12:435–76
30. Mougin G, Magnaudet J. 2001. *Phys. Rev. Lett.* 88:014502
31. Hunt JCR, Perkins R, Fung J. 1994. *Multiph. Sci. Technol.* 8:595–643
32. Mathai V, Calzavarini E, Brons J, Sun C, Lohse D. 2016. *Phys. Rev. Lett.* 117:024501
33. Douady S, Couder Y, Brachet ME. 1991. *Phys. Rev. Lett.* 67:983–86
34. La Porta A, Voth GA, Crawford AM, Alexander J, Bodenschatz E. 2001. *Nature* 409:1017–19
35. Wang LP, Maxey MR. 1993. *Appl. Sci. Res.* 51:291–96
36. Spelt P, Biesheuvel A. 1997. *J. Fluid Mech.* 336:221–44
37. Calzavarini E, Kerscher M, Lohse D, Toschi F. 2008. *J. Fluid Mech.* 607:13–24
38. Calzavarini E, Cencini M, Lohse D, Toschi F. 2008. *Phys. Rev. Lett.* 101:084504
39. Monchaux R, Bourgoin M, Cartellier A. 2010. *Phys. Fluids* 22:103304
40. Tagawa Y, Mercado JM, Prakash VN, Calzavarini E, Sun C, Lohse D. 2012. *J. Fluid Mech.* 693:201–15
41. Fiabane L, Zimmermann R, Volk R, Pinton JF, Bourgoin M. 2012. *Phys. Rev. E* 86:035301
42. Obligado M, Teitelbaum T, Cartellier A, Mininni P, Bourgoin M. 2014. *J. Turbul.* 15:293–310
43. Volk R, Calzavarini E, Verhille G, Lohse D, Mordant N, et al. 2008. *Physica D* 237:2084–89
44. Volk R, Mordant N, Verhille G, Pinton JF. 2008. *Europhys. Lett.* 81:34002
45. Voth GA, La Porta A, Crawford AM, Alexander J, Bodenschatz E. 2002. *J. Fluid Mech.* 469:121–60
46. Csanady G. 1963. *J. Atmos. Sci.* 20:201–8
47. Maxey M. 1987. *J. Fluid Mech.* 174:441–65
48. Parishani H, Ayala O, Rosa B, Wang LP, Grabowski W. 2015. *Phys. Fluids* 27:033304
49. Bodenschatz E, Malinowski SP, Shaw RA, Stratmann F. 2010. *Science* 327:970–71
50. Magnaudet J, Eames I. 2000. *Annu. Rev. Fluid Mech.* 32:659–708
51. Mathai V, Huisman SG, Sun C, Lohse D, Bourgoin M. 2018. *Phys. Rev. Lett.* 121:054501
52. Sridhar G, Katz J. 1995. *Phys. Fluids* 7:389–99
53. Tio KK, Liñán A, Lasheras JC, Gañán-Calvo AM. 1993. *J. Fluid Mech.* 254:671–99
54. Aliseda A, Lasheras J. 2011. *Phys. Fluids* 23:093301
55. Deane GB, Stokes MD. 2002. *Nature* 418:839–44
56. Duineveld P. 1995. *J. Fluid Mech.* 292:325–32
57. Ryskin G, Leal LG. 1984. *J. Fluid Mech.* 148:19–35
58. Naso A, Prosperetti A. 2010. *New J. Phys.* 12:033040

59. Chouippe A, Uhlmann M. 2015. *Phys. Fluids* 27:123301
60. Loisy A, Naso A. 2017. *Phys. Rev. Fluids* 2:014606
61. Naso A, Pumir A. 2005. *Phys. Rev. E* 72:056318
62. Xu H, Pumir A, Falkovich G, Bodenschatz E, Shats M, et al. 2014. *PNAS* 111:7558–63
63. Mougin G, Magnaudet J. 2006. *J. Fluid Mech.* 567:185–94
64. Mathai V, Neut MWM, van der Poel EP, Sun C. 2016. *Exp. Fluids* 57:1–10
65. Mathai V, Zhu X, Sun C, Lohse D. 2018. *Nat. Commun.* 9:1792
66. Brücker C. 1999. *Phys. Fluids* 11:1781–96
67. Mathai V, Zhu X, Sun C, Lohse D. 2017. *Phys. Rev. Lett.* 119:054501
68. Risso F. 2017. *Annu. Rev. Fluid Mech.* 50:25–48
69. Ford B, Loth E. 1998. *Phys. Fluids* 10:178–88
70. Lamb H. 1993. *Hydrodynamics*. Cambridge, UK: Cambridge Univ. Press
71. Galper A, Miloh T. 1995. *J. Fluid Mech.* 295:91–120
72. Mougin G, Magnaudet J. 2002. *Int. J. Multiph. Flow* 28:1837–51
73. Auguste F, Magnaudet J. 2018. *J. Fluid Mech.* 841:228–66
74. Cano-Lozano JC, Martinez-Bazan C, Magnaudet J, Tchoufag J. 2016. *Phys. Rev. Fluids* 1:053604
75. Wu M, Gharib M. 2002. *Phys. Fluids* 14:L49–52
76. Mazzitelli IM, Lohse D. 2004. *New J. Phys.* 6:203
77. Ravelet F, Colin C, Risso F. 2011. *Phys. Fluids* 23:103301
78. Zimmermann R, Gasteuil Y, Bourgoin M, Volk R, Pumir A, et al. 2011. *Rev. Sci. Instrum.* 82:033906
79. Zimmermann R, Gasteuil Y, Bourgoin M, Volk R, Pumir A, Pinton JF. 2011. *Phys. Rev. Lett.* 106:154501
80. Bellani G, Variano EA. 2012. *New J. Phys.* 14:125009
81. Faxén H. 1922. *Ann. Phys.* 373:89–119
82. Mathai V, Prakash VN, Brons J, Sun C, Lohse D. 2015. *Phys. Rev. Lett.* 115:124501
83. Govardhan RN, Williamson CHK. 2005. *J. Fluid Mech.* 531:11–47
84. Zhang W, Stone H. 1998. *J. Fluid Mech.* 367:329–58
85. Zenit R, Magnaudet J. 2008. *Phys. Fluids* 20:061702
86. Loth E, Dorgan AJ. 2009. *Environ. Fluid Mech.* 9:187–206
87. Loth E. 2008. *AIAA J.* 46:801–9
88. Loth E. 2008. *Int. J. Multiph. Flow* 34:523–46
89. Van Nierop EA, Luther S, Bluemink JJ, Magnaudet J, Prosperetti A, Lohse D. 2007. *J. Fluid Mech.* 571:439–54
90. Legendre D, Magnaudet J. 1998. *J. Fluid Mech.* 368:81–126
91. Legendre D, Magnaudet J. 1997. *Phys. Fluids* 9:3572–74
92. Takemura F, Takagi S, Magnaudet J, Matsumoto Y. 2002. *J. Fluid Mech.* 461:277–300
93. So S, Morikita H, Takagi S, Matsumoto Y. 2002. *Exp. Fluids* 33:135–42
94. Kitagawa A, Sugiyama K, Murai Y. 2004. *Int. J. Multiph. Flow* 30:1213–34
95. van Sint Annaland M, Dijkhuizen W, Deen N, Kuipers J. 2006. *AIChE J.* 52:99–110
96. Zhang D, Deen N, Kuipers J. 2006. *Chem. Eng. Sci.* 61:7593–608
97. Nakoryakov V, Kashinsky O, Burdukov A, Odnoral V. 1981. *Int. J. Multiph. Flow* 7:63–81
98. Kashinsky O, Randin V. 1999. *Int. J. Multiph. Flow* 25:109–38
99. Drew DA, Lahey RT Jr. 1993. In *Particulate Two-Phase Flow*, ed. MC Roco, pp. 509–66. Boston: Butterworth-Heinemann
100. Lu J, Biswas S, Tryggvason G. 2006. *Int. J. Multiph. Flow* 32:643–60
101. Tryggvason G, Lu J. 2015. *Mech. Eng. Rev.* 2:1–14
102. Dabiri S, Lu J, Tryggvason G. 2013. *Phys. Fluids* 25:102110
103. Tomiyama A, Tamai H, Zun I, Hosokawa S. 2002. *Chem. Eng. Sci.* 57:1849–58
104. Batchelor GK. 1953. *The Theory of Homogeneous Turbulence*. Cambridge, UK: Cambridge Univ. Press
105. Lance M, Bataille J. 1991. *J. Fluid Mech.* 222:95–118
106. Martínez-Mercado J, Palacios-Morales CA, Zenit R. 2007. *Phys. Fluids* 19:103302
107. Roghair I, Mercado JM, Annaland MVS, Kuipers H, Sun C, Lohse D. 2011. *Int. J. Multiph. Flow* 37:1093–98

108. Riboux G, Legendre D, Risso F. 2013. *J. Fluid Mech.* 719:362–87

108a. Pandey V, Ramadugu R, Perlekar P. 2019. arXiv:1910.01936

108b. Prakash VN, Mercado JM, van Wijngaarden L, Mancilla E, Tagawa Y, et al. 2016. *Fluid Mech.* 791:174–90

109. Mazzitelli IM, Lohse D. 2009. *Phys. Rev. E* 79:066317

110. Rensen J, Luther S, Lohse D. 2005. *J. Fluid Mech.* 538:153–87

111. Van Wijngaarden L. 1998. *Theor. Comput. Fluid Dyn.* 10:449–58

112. Alméras E, Mathai V, Lohse D, Sun C. 2017. *J. Fluid Mech.* 825:1091–112

113. du Cluzeau A, Bois G, Toutant A. 2019. *J. Fluid Mech.* 866:132–68

114. Jeong J, Hussain F. 1995. *J. Fluid Mech.* 285:69–94

115. Alméras E, Mathai V, Sun C, Lohse D. 2019. *Int. J. Multiph. Flow* 114:316–22

116. Riboux G, Risso F, Legendre D. 2010. *J. Fluid Mech.* 643:509–39

117. Pumir A. 1996. *Phys. Fluids* 8:3112–27

118. Champagne F, Harris V, Corrsin S. 1970. *J. Fluid Mech.* 41:81–139

119. Gualtieri P, Battista F, Casciola C. 2015. *J. Phys. Conf. Ser.* 656:012018

120. Rosti ME, Ge Z, Jain SS, Dodd MS, Brandt L. 2019. *J. Fluid Mech.* 876:962–84

121. Kawamura T, Nakatani T. 2006. In *Proceedings of the ASME 2006 2nd Joint US–European Fluids Engineering Summer Meeting Collocated with the 14th International Conference on Nuclear Engineering*, pp. 1571–78. New York: ASME

122. Madavan N, Deutsch S, Merkle C. 1984. *Phys. Fluids* 27:356–63

123. Madavan N, Deutsch S, Merkle C. 1985. *J. Fluid Mech.* 156:237–56

124. Gutierrez-Torres C, Hassan Y, Jimenez-Bernal JA. 2008. *J. Fluids Eng.* 130:111304

125. Sanders WC, Winkel ES, Dowling DR, Perlin M, Ceccio SL. 2006. *J. Fluid Mech.* 552:353–80

126. Xu J, Maxey MR, Karniadakis GE. 2002. *J. Fluid Mech.* 468:271–81

127. Ferrante A, Elghobashi S. 2004. *J. Fluid Mech.* 503:345–55

128. Lu J, Fernández A, Tryggvason G. 2005. *Phys. Fluids* 17:095102

129. Murai Y. 2014. *Exp. Fluids* 55:1–10

130. Rawat S, Chouippe A, Zamansky R, Legendre D, Climent E. 2019. *Comput. Fluids* 178:73–87

131. Serizawa A, Kataoka I, Michiyoshi I. 1975. *Int. J. Multiph. Flow* 2:235–46

132. Antal S, Lahey R Jr., Flaherty J. 1991. *Int. J. Multiph. Flow* 17:635–52

133. Unverdi S, Trygvasson G. 1992. *J. Comput. Phys.* 100:25–37

134. Lu J, Tryggvason G. 2008. *Phys. Fluids* 20:040701

135. Tryggvason G, Scardovelli R, Zaleski S. 2011. *Direct Numerical Simulations of Gas–Liquid Multiphase Flows*. Cambridge, UK: Cambridge Univ. Press

136. Lu J, Tryggvason G. 2006. *Phys. Fluids* 18:103302

137. Dabiri S, Bhuvankar P. 2016. *Phys. Fluids* 28:062101

138. Lu J, Muradoglu M, Tryggvason G. 2017. *Int. J. Multiph. Flow* 95:135–43

139. Clift R, Grace J, Weber M. 1978. *Bubbles, Drops, and Particles*. New York: Academic

140. Takagi S, Matsumoto Y. 2011. *Annu. Rev. Fluid Mech.* 43:615–36

141. Guet S, Ooms G. 2006. *Annu. Rev. Fluid Mech.* 38:225–49

142. Besagni G, Inzoli F. 2016. *Chem. Eng. Sci.* 146:259–90

143. Grossmann S, Lohse D, Sun C. 2016. *Annu. Rev. Fluid Mech.* 48:53–80

144. Verschoof RA, Van Der Veen RC, Sun C, Lohse D. 2016. *Phys. Rev. Lett.* 117:104502

145. Murai Y, Oiwa H, Takeda Y. 2005. *J. Phys. Conf. Ser.* 14:143–56

146. Murai Y, Oiwa H, Takeda Y. 2008. *Phys. Fluids* 20:034101

147. van den Berg TH, Luther S, Lathrop DP, Lohse D. 2005. *Phys. Rev. Lett.* 94:044501

148. van Gils DP, Narezo Guzman D, Sun C, Lohse D. 2013. *J. Fluid Mech.* 722:317–47

149. Chouippe A, Climent E, Legendre D, Gabillet C. 2014. *Phys. Fluids* 26:043304

150. Fokoua GN, Gabillet C, Aubert A, Colin C. 2015. *Phys. Fluids* 27:034105

151. Sugiyama K, Calzavarini E, Lohse D. 2008. *J. Fluid Mech.* 608:21–41

152. Spandan V, Ostilla-Mónico R, Verzicco R, Lohse D. 2016. *J. Fluid Mech.* 798:411–35

153. Zhu X, Ostilla-Mónico R, Verzicco R, Lohse D. 2016. *J. Fluid Mech.* 794:746–74

154. Marcus PS. 1984. *J. Fluid Mech.* 146:65–113
155. Fardin M, Perge C, Taberlet N. 2014. *Soft Matter* 10:3523–35
156. Andereck CD, Liu SS, Swinney HL. 1986. *J. Fluid Mech.* 164:155–83
157. Spandan V, Verzicco R, Lohse D. 2018. *J. Fluid Mech.* 849:R3
158. Benzi R, Ching ES. 2018. *Annu. Rev. Condens. Matter Phys.* 9:163–81
159. Procaccia I, L'vov VS, Benzi R. 2008. *Rev. Mod. Phys.* 80:225–47
160. White CM, Mungal MG. 2008. *Annu. Rev. Fluid Mech.* 40:235–56
161. Eckhardt B, Grossmann S, Lohse D. 2007. *Europhys. Lett.* 78:24001
162. Deckwer WD. 1980. *Chem. Eng. Sci.* 35:1341–46
163. Wang Z, Mathai V, Sun C. 2019. *Nat. Commun.* 10:3333
164. Alards KM, Kunnen RP, Clercx HJ, Toschi F. 2019. arXiv:1907.00049 [cond-mat.soft]
165. Zhong JQ, Funfschilling D, Ahlers G. 2009. *Phys. Rev. Lett.* 102:124501
166. Lakkaraju R, Stevens RJ, Oresta P, Verzicco R, Lohse D, Prosperetti A. 2013. *PNAS* 110:9237–42
167. Sekoguchi K, Nakazatomi M, Sato Y, Tanaka O. 1980. *Bull. JSME* 23:1625–31
168. Sato Y, Sadatomi M, Sekoguchi K. 1981. *Int. J. Multiph. Flow* 7:167–77
169. Sato Y, Sadatomi M, Sekoguchi K. 1981. *Int. J. Multiph. Flow* 7:179–90
170. Dabiri S, Tryggvason G. 2015. *Chem. Eng. Sci.* 122:106–13
171. Kitagawa A, Kosuge K, Uchida K, Hagiwara Y. 2008. *Exp. Fluids* 45:473–84
172. Kitagawa A, Uchida K, Hagiwara Y. 2009. *Int. J. Heat Fluid Flow* 30:778–88
173. Kitagawa A, Murai Y. 2013. *Chem. Eng. Sci.* 99:215–24
174. Deen NG, Kuipers J. 2013. *Chem. Eng. Sci.* 102:268–82

Contents

Errata

An online log of corrections to *Annual Review of Condensed Matter Physics* articles may
be found at http://www.annualreviews.org/errata/conmatphys